

Deconvolution of the point spread function of an x-ray image intensifier

by

Sarat Kakumanu

A Thesis Submitted to the
Graduate Faculty in Partial Fulfillment of the
Requirements for the Degree of
MASTER OF SCIENCE

Department: Electrical Engineering and Computer Engineering
Major: Electrical Engineering

Approved:

In Charge of Major Work

For the Major Department

For the Graduate College

Members of the Committee:

Iowa State University
Ames, Iowa
1994

Copyright © Sarat Kakumanu, 1994. All rights reserved.

TABLE OF CONTENTS

DEDICATION	ix
ACKNOWLEDGEMENTS	x
CHAPTER 1. INTRODUCTION	1
Research Objective	3
Overview of Chapters	3
CHAPTER 2. IMAGE INTENSIFIER CALIBRATION	5
Principle of Operation of an Image Intensifier	8
Input conversion screen	10
Electromagnetic lens	11
Output conversion screen	12
Flux Measurement of the X-ray Generator	13
Calibration of Sodium Iodide Detector	18
Calibration Plots for the X-ray II-TV System	20
CHAPTER 3. A MODEL FOR REAL-TIME X-RAY IMAGING .	34
X-ray Simulation Fundamentals	34
Initial x-ray beam modeling	34
X-ray beam and target object interaction modeling	36

Modeling Pincushion Distortion	39
Incorporation of Blur	41
Addition of Noise	44
CHAPTER 4. IMAGE RESTORATION	50
Preliminaries	50
Different Restoration Filters	52
Pseudo inverse filter	52
Wiener filter	54
Iterative Wiener filter	58
Iterative Wiener filter with an additive correction factor	62
A filter based on the EM algorithm	68
FIER MEM filter	70
Comparison of various filters	80
CHAPTER 5. CONCLUSIONS AND FUTURE WORK	82
Ideas for future work	86
BIBLIOGRAPHY	87

LIST OF TABLES

Table 4.1:	Mean Square Error between the ideal and restored images for different filters	81
------------	--	----

LIST OF FIGURES

Figure 2.1:	X-ray Imaging	5
Figure 2.2:	Schematic diagram of an Image Intensifier	9
Figure 2.3:	Plot of the spectrum from a NaI detector at 100 KeV, 0.01 mA	14
Figure 2.4:	Plot of the spectra from a NaI detector at different KeV . . .	15
Figure 2.5:	Calibration curve for the NaI detector	19
Figure 2.6:	Real time X-ray system	21
Figure 2.7:	X-ray - Image Intensifier System	22
Figure 2.8:	Imaging system	23
Figure 2.9:	Calibration curves for the X-ray Image Intensifier	24
Figure 2.10:	Calibration curves for the imaging system using the sony cam- era	26
Figure 2.11:	Calibration curves for the imaging system using red, green, yellow LEDs and an incandescent lamp for the sony camera .	27
Figure 2.12:	Calibration curves for the imaging system using red, green, yellow LEDs and an incandescent lamp for the vidicon camera	28
Figure 2.13:	Calibration curves for the imaging system using red, green, yellow LEDs and an incandescent lamp for the CID camera .	29

Figure 2.14:	Calibration curves for the imaging system using different cameras for a green LED	30
Figure 2.15:	Calibration curve for the imaging system using the 8-bit CCD camera and the green LED	32
Figure 2.16:	Calibration curves for the real time X-ray system	33
Figure 3.1:	X-ray Simulation	35
Figure 3.2:	Ideal x-ray image of the turbine blade	38
Figure 3.3:	Thresholded pincushion distortion image	40
Figure 3.4:	Pincushion distorted x-ray image of the turbine blade	42
Figure 3.5:	Numerical derivative of smoothed edge scan data (noise-like signal), with overplot of fitted Gaussian (smooth signal)	45
Figure 3.6:	Blurred x-ray image of the turbine blade	46
Figure 3.7:	Blurred, pincushion distorted and noisy x-ray image of the turbine blade	48
Figure 3.8:	Real time x-ray image of the turbine blade	49
Figure 4.1:	Ideal Image	55
Figure 4.2:	Slice across the Ideal Image	55
Figure 4.3:	Blurred and pseudo-inverse filtered images	56
Figure 4.4:	Input and Pseudo-inverse processed slice profiles	56
Figure 4.5:	Real-time image of a resolution gauge	57
Figure 4.6:	Pseudo-inverse filtered images of the resolution gauge	57
Figure 4.7:	Input and Pseudo-inverse processed slice profiles of the resolution gauge	57

Figure 4.8:	Blurred and Wiener filtered images	59
Figure 4.9:	Input and Wiener filter processed slice profiles	59
Figure 4.10:	Real-time and Wiener filtered images of the resolution gauge	60
Figure 4.11:	Input and Wiener filter processed slice profiles of the resolution gauge	60
Figure 4.12:	Blurred and iterative Wiener filtered images	63
Figure 4.13:	Input and iterative Wiener filter processed slice profiles . . .	63
Figure 4.14:	Real-time and iterative Wiener filtered images of the resolution gauge	64
Figure 4.15:	Input and iterative Wiener filter processed slice profiles of the resolution gauge	64
Figure 4.16:	Blurred image and a processed image using an iterative Wiener filter with an additive correction factor	66
Figure 4.17:	Input and iterative Wiener filter with an additive correction processed slice profiles	66
Figure 4.18:	Real-time image and a processed image of the resolution gauge using an iterative Wiener filter with an additive correction factor	67
Figure 4.19:	Input and Iterative wiener filter with an additive correction factor processed slice profiles of the resolution gauge	67
Figure 4.20:	Blurred and EM filtered images	71
Figure 4.21:	Input and EM filter processed slice profiles	71
Figure 4.22:	Real-time and EM filtered images of the resolution gauge . .	72
Figure 4.23:	Input and EM filter processed slice profiles of the resolution gauge	72

Figure 4.24: Block diagram of the FIER MEM filter	77
Figure 4.25: Blurred and MEM filtered images	78
Figure 4.26: Input and MEM filter processed slice profiles	78
Figure 4.27: Real-time and MEM filtered images of the resolution gauge .	79
Figure 4.28: Input and MEM filter processed slice profiles of the resolution gauge	79
Figure 5.1: Image of a circular gauge with a larger field of view	84
Figure 5.2: Deconvoluted image of a circular gauge with a larger field of view	84
Figure 5.3: Image of a circular gauge with a smaller field of view	85
Figure 5.4: Deconvoluted image of a circular gauge with a smaller field of view	85

DEDICATION

To my parents

ACKNOWLEDGEMENTS

Firstly, I would like to thank my major advisor Dr. Joe Gray for his constant support and encouragement throughout my work for this thesis. I wish to thank my co-major advisor Dr. Satish Udpa for giving me useful suggestions throughout my thesis. I would also like to thank my committee members Dr. Lalita Udpa and Dr. Dick Wallingford for their valuable time. A special thanks to Dr. Terry Jensen for his help in difficult situations. I am also grateful to a number of people at the Center for NDE. To mention a few - Ed Doering, Vivekanand Kini, Liz Siwek, Jason Ting and Kasivisvanath Rangarajan.

Finally, I would like to thank my parents and brothers without whose constant encouragement this work wouldn't have been possible.

This material is based upon work performed at the FAA Center for Aviation Systems Reliability operated by Iowa State University and supported by the Federal Aviation Administration under Grant No. 93-G-018. Any opinions, findings, conclusions or recommendations expressed in this material are those of the author and do not necessarily reflect the views of the Federal Aviation Administration.

CHAPTER 1. INTRODUCTION

Nondestructive Evaluation (NDE) is an interdisciplinary branch that is concerned with ensuring the quality and serviceability of materials and structures. The science of NDE incorporates the technology necessary for detection and measurement of significant properties, including discontinuities, in items ranging from research specimens to finished products. By definition, nondestructive techniques are the means by which materials and structures may be inspected without impairment of their serviceability. Using NDE, internal properties of hidden flaws can be revealed or inferred using appropriate techniques.

NDE is performed on a wide variety of materials including metals, ceramics, epoxies, wood, fiber glass, and composites. Many types of NDE techniques have been developed; they are differentiated primarily on how they introduce energy into the material and measure the result. The types of energy involved include acoustic (ultrasonic and acoustic emission), electromagnetic (magnetostatic, eddy currents, microwaves, optics, X-rays, and gamma rays), neutrons and heat waves.

One of the most widely used techniques for the inspections of components in industry is real-time X-ray radiography. Consequently there is a considerable interest in the quantitative modeling of the underlying physical phenomenon. However, with the advent of new hardware in the form of microfocus X-ray generators and

image intensifier based real time imaging systems, further interest has been stirred in developing an understanding of the image generation process caused by penetrating radiation. In addition the, increasing complexity and tighter tolerances associated with manufactured components are pushing the limits of the traditional inspection techniques. In order to improve the limits of inspectability it is essential to have accurate tools for the qualitative and quantitative models characterizing the underlying physical process. The successful development of a quantitative model will provide the necessary tools for simulation of realistic radiographic inspection scenario. The ability to perform inspection simulations of a part, while it is at the design stage, greatly aids in assuring that the prescribed techniques of inspection are adequate.

For NDE inspections using X-ray radiography either a film or a real-time detector employing an image intensifier can be used as the detector. Film has the advantages of high resolution, high dynamic range (100:1), long integration time which reduces quantum mottle noise, and archival capability. Resolution is measured in terms of spatial frequency, with units of line pairs (lp) per unit distance (e.g., lp/mm). Film resolution of 10 to 20 lp/mm (Halmshaw, 1987) are easily possible. The disadvantage of using film is the need for chemical processing to develop and fix the image. This process takes at least three minutes, and results in a static image. Real-time detectors allow the X-ray field to be viewed continuously. Consequently the sample can be inspected rapidly under a wide variety of orientations. This advantage is offset by the real-time detector's lower resolution of 3-6 lp/mm (Halmshaw, 1987) and lower dynamic range of 20:1 (Gupta and Krohn, 1987). Furthermore, real-time converters inherently do not have any integration capability. However this can be overcome using digital integration (i.e. frame averaging) techniques. For these reasons, NDE

practitioners prefer film.

Research Objective

The purpose of this research is to improve the quality of image-intensifier based real-time X-ray systems by removing the blur introduced due to the intensifier and other elements in the imaging chain. Also, a qualitative and quantitative comparison of the different restoration filters is made. The performance of the various filters is evaluated and presented. To further aid in the restoration process a quantitative model for real-time X-ray inspection is developed. The model development is divided into three steps. The first step is to obtain a calibration curve for the X-ray image intensifier system. The second step is to measure the point spread function (PSF) of the system while the third step involves measurement of the pincushion distortion characteristics of the system. The thesis demonstrates the use of the model in restoring images.

Overview of Chapters

Chapter 2 describes the principle of operation of the image intensifier and the calibration procedure. It explains the experimental setup needed to measure the calibration curves for the image-intensifier based real-time X-ray imaging system. Chapter 3 describes the steps involved in developing a model for the real-time X-ray system. After describing the model developed for film radiography the thesis presents a model for the real-time detector. Experimental procedures for measuring the point spread function and pincushion distortion and methods for incorporating the information into the overall model are explained. Chapter 4 investigates the

effect of various deconvolution routines on the image quality of an X-ray image. Both quantitative and qualitative comparisons of the filters are made in this section. Chapter 5 summarizes the work, presents conclusions, and describes future directions for research.

CHAPTER 2. IMAGE INTENSIFIER CALIBRATION

Figure 2.1 shows a simple diagram of a typical X-ray imaging system. In this process the object is illuminated by a uniform X-ray beam (X). The X-rays penetrate the object and experience absorption and arrive at the detector. The absorption is a function of the thickness, the absorption coefficient of the material and the energy of the photon. Therefore an object that has a varying thickness or contains an

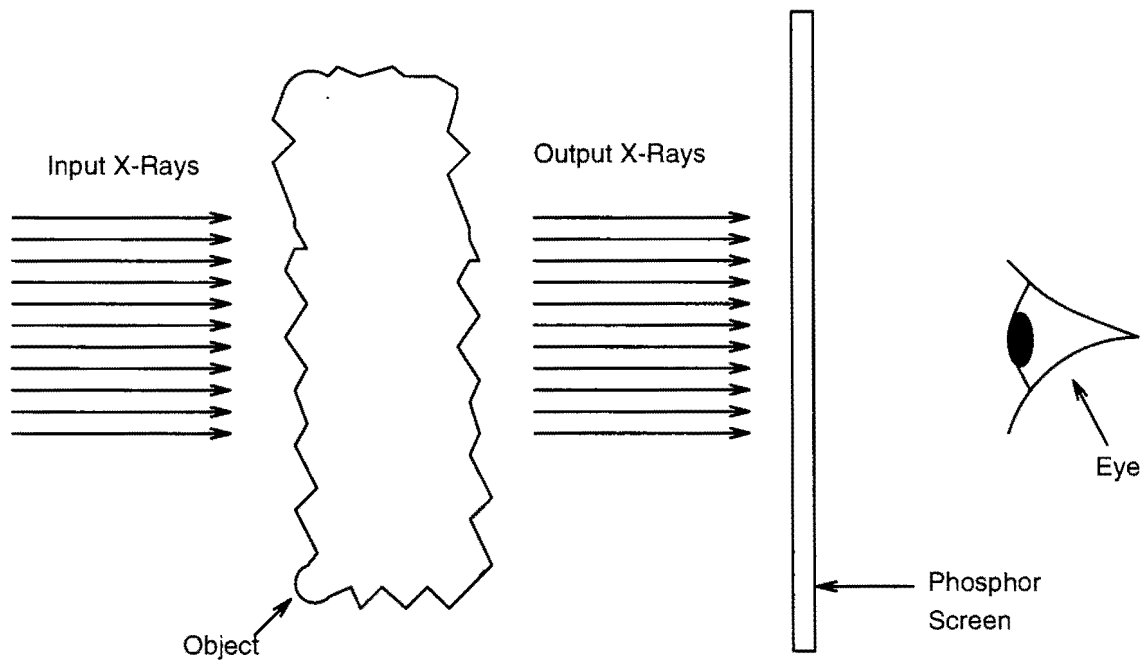


Figure 2.1: X-ray Imaging

inhomogeneity in its structure results in local intensity variations at the detection plane. The beam-intensity pattern produced by these variations is made visible by conversion of the X-rays into visible light by a fluorescent screen. In this manner the structural details of the object are displayed in terms of brightness variation. Simple X-ray fluoroscopy as described above, has the drawback of requiring a high-intensity X-ray source. In addition, the fluorescent image is brightness and quantum noise limited. A variety of designs are available to improve the fluoroscopic process. The main design issues are sensitivity to photons in the X-ray region (≥ 10 KeV), amplification that is adequate for viewing by an optical video camera, high spatial linearity, and good resolution. The image intensifier tube is commonly used to accomplish these goals in medical and industrial applications. It operates by converting the electrically neutral X-ray photons to electrons via the photo-electric effect. The electrons are then accelerated and focused by an electromagnetic lens onto a small phosphor to generate an optical image. This design has relatively high resolution and sensitivity, and good conversion efficiency. In contrast to film however, however, it results in greater geometric distortion and offers relatively limited levels of resolution. Before providing a detailed description of the image intensifier a comparison of other X-ray detectors is made.

In one of the commercial designs, a microchannel plate (MCP) is incorporated in an X-ray intensifier tube by combining it with a planar X-ray image converter. The converter transforms the local density variations of the X-ray flux into an electronic image that is intensified by the MCP and displayed on an output screen. The plate is used instead of employing an electromagnetic lens in the image intensifier. A MCP (Chalmeton, 1980) is formed when a large number of microchannel tubes are fused

together. A microchannel is a small-diameter tube made of semiconducting lead glass that is covered by a secondary electron emission layer. When voltage of about 1000 Volts is applied a longitudinal electric field is produced inside the tube. When an electron strikes the channel input, it generates two or three secondary electrons which enter the electric field. These electrons after acceleration strike the wall again, producing more secondary electrons and so on. The total gain of this multiplication process is usually 10^4 to 10^5 . The total transit time of the electrons from the converter plate, to the fluorescent screen through the microchannel plate is very fast (2 to 3 ns). Hence response time of such an intensifier is in fact limited by the response time of the input X-ray converter and the output phosphor screen. Microchannel plates result in low geometric distortion. The main disadvantage lies in the excessive cost of channel plates, particularly in the case of large diameter plates. These plates are expensive since they are produced in relatively small quantities. They are also less reliable than the smaller ones.

Some designs couple the photodetector array directly to the scintillation material. Zhu, Babot, and Piex (1990) compared the performance of a 1-D 1024 array of photodiodes coupled with a scintillator to an image intensifier and found 50% improvement in resolution, 20 dB increase in signal to noise ratio, and 20% improvement in sensitivity. The 1-D array must be scanned to create a 2-D image. Since this process takes about 4 seconds, the improved performance comes at the cost of frame speed.

The photodiode can also be used directly to detect low energy (≤ 10 KeV) X-rays. Samuelson and Jaggi (1989) used a commercially available 256×256 photodiode array in an X-ray microscopy application. They found that using a large pixel

pitch of 40 μm was required to minimize cross-talk between the pixels. Photodiodes also provide integration capability of up to 1 hour when cooled to minimize thermal electron noise. This design is free of geometric distortion.

The digital phosphor system (Hillen, Schiebel, and Zaengel, 1987) uses a photo-stimulable phosphor as the X-ray detector. The X-ray photon energy is temporarily stored within the crystal lattice since thermal energy is insufficient to cause the luminescent center to release the excess energy. A small diameter laser beam is scanned over the phosphor plate. The laser adds enough energy to cause the material to release the stored energy as optical photons. The local variation in emission intensity is proportional to the absorbed X-ray energy. The optical photons pass through a light guide and are converted to an electron current by a photomultiplier tube. This current is amplified and digitized to make the final image. The phosphor screen has blurring due to optical scattering just as in an image intensifier and so the resolution of the storage phosphor system is the same ($\leq 4\text{lp/mm}$). However, this system has higher dynamic range since the laser readout system can be adjusted to match the X-ray exposure level. The storage phosphor has inherent integration capability like X-ray film, and has minimal geometric distortion.

Principle of Operation of an Image Intensifier

An X-ray Image Intensifier (XRII) is used as the detector for work reported in this thesis. Figure 2.2 shows the basic construction of an XRII tube. This device converts an incident X-ray flux to an optical image which is recorded by a video camera. The input scintillator screen is made of a phosphorescent material which converts the high energy X-ray photons to lower energy optical photons. Since the

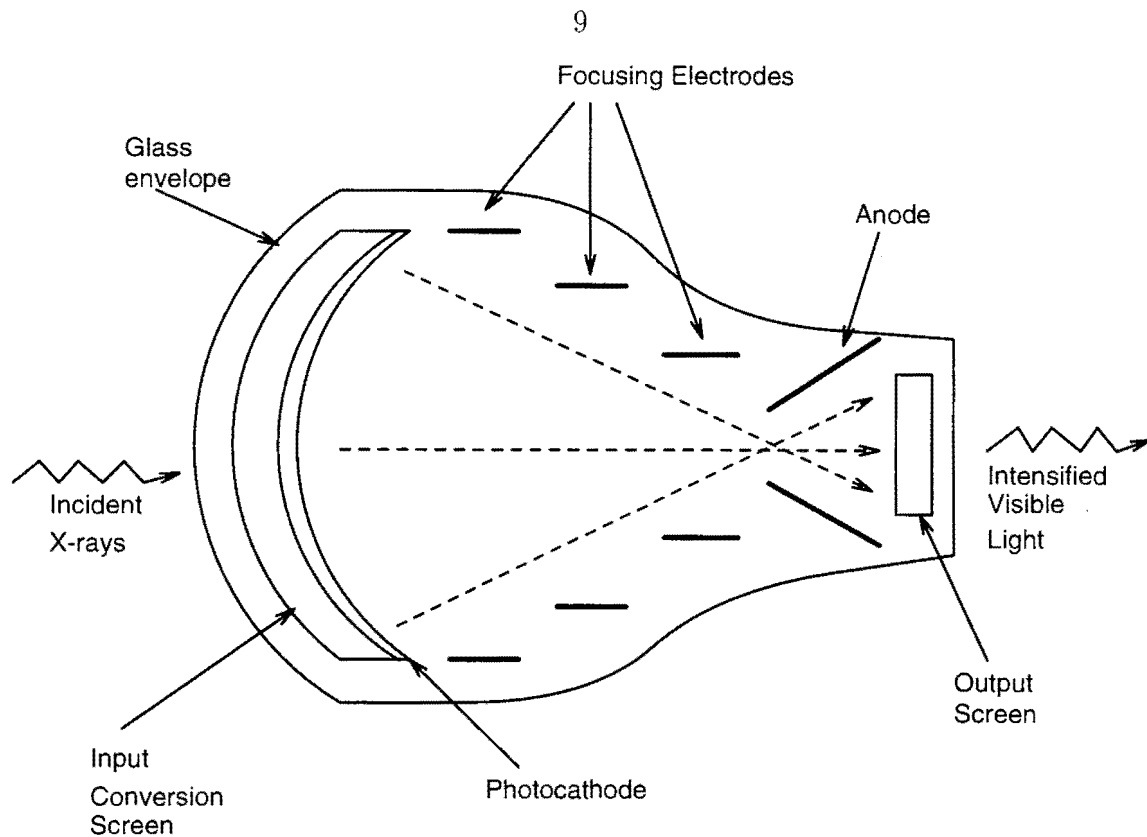


Figure 2.2: Schematic diagram of an Image Intensifier

brightness of the optical image is very weak (typically only 1% of the incident X-ray photons are converted), intensification is used to increase the brightness. Photons are electrically neutral and cannot be amplified or manipulated using electromagnetic fields. The intensification process begins at the photocathode which converts the low energy photons to electrons using the photoelectric effect. These electrons are accelerated at 20 - 30 KeV towards an output conversion phosphor that is 10 times small in diameter than the input conversion screen. Thus the image is intensified by electron acceleration and image minification. The following sections describe this complete process in greater detail.

Input conversion screen

The input conversion screen consists of a thin layer of phosphor material. Early generation tubes used zinc sulfide (ZnS) or cadmium sulfide (CdS) as the phosphor material. Since the early 1980's, cesium iodide doped with a sodium impurity (CsI(Na)) has been the material of choice. It is more sensitive to X-rays and its material characteristics permit deposition of thinner screens which results in higher resolution (Bates, 1980). Resolution is inversely proportional to screen thickness. In the case of a thicker screen, the optical photons have a greater scattering volume. This scattering process is known as phosphor bloom. Sensitivity, on the other hand, is directly proportional to screen thickness. Here, each X-ray photon has a greater chance of interacting with a greater volume of phosphor material resulting in greater conversion efficiency. Thus, there is a fundamental trade-off between sensitivity and resolution. Special techniques have been used to reduce the phosphor bloom by growing the CsI crystals as thin needle-shaped elements (Link et al., 1989). In this case the crystals act like optic fibers and cross-talk between the crystals is reduced.

The conversion screen is curved in a spherical shape to ensure that the path length between all parts of the input screen and the output conversion screen is equal to minimize distortion (Csorba, 1985). However, this curvature results in a distortion when a flat object is mapped onto the curved screen. The image magnification increases off-axis, resulting in "pincushion" distortion. This has the effect of making parallel lines in the object plane bow to the center of the image in the detected image plane. Furthermore the pincushion distortion is dependent on the position of the X-ray source, resulting in view-dependent distortion (Chackraborty, 1987). Any measurement procedure which uses multiple sources or translation of a single source

must take this factor into account. Pincushion distortion is the dominant spatial distortion encountered when an image intensifier tube is used.

The increase in magnification at off-axis locations also contributes to vignetting. This is a radiometric distortion where the image of a uniform intensity source has decreased gray levels at the periphery of the image. This effect was found to contribute to a 30 % reduction for the image intensifier used here. Older generation tubes have had reductions as high as 50 % (Casperson, Spiegler, Grollman, 1976). The scintillator is mechanically coupled to a photocathode. This photocathode uses the photoelectric effect to convert the output photons of the scintillator to electrons. Photocathode materials sense optical radiation with wavelengths in the range 1200 - 120 nm, or approximately 0.01 - 0.1 KeV (Csorba, 1985), so the input scintillator is required to "downconvert" the energy of the X-ray photons (10 - 200 KeV) into this regime. The electron field is proportional to the input X-ray field, and is input to the electromagnetic lens for amplification.

Electromagnetic lens

The electrons released by the photocathode are accelerated at 30 KeV towards the output conversion screen. This acceleration is the first step in the intensification of the X-ray image. The output conversion screen is also 10 times smaller in diameter than the input conversion screen. The electromagnetic lens focuses all photocathode electrons onto the output screen. Image minification is the second step in the intensification process. The overall increase in brightness is on the order of 10^4 (Christensen, Curry and Nunnally, 1972). The focusing quality of the electromagnetic lens steadily degrades away from the central axis (Csorba, 1985). Curving the input conversion

screen alleviates this problem to a certain extent, but image sharpness is still a maximum in the center of the image. For this reason, the electron lens of multi-field image intensifiers is externally adjustable to map reduced portions of the input screen onto the output screen. For example, a 9" tri-field image intensifier has 4.5", 6" and 9" operation modes. This permits the operator to conveniently change the field of view. The smaller fields use a restricted area in the center of the tube where electron focusing is better and geometric distortion is reduced. However, this reduced field of view implies that a smaller portion of the sample can be inspected at a time. Spiral distortion is another aberration introduced by the electromagnetic lens. Inhomogeneities in the lens field as well as external magnetic fields cause straight lines in the object plane to be warped into S-shaped curves.

Output conversion screen

The output phosphor is a circular screen that is typically 15 to 20 mm in diameter. The output phosphor limits the overall resolution. Due to the ten-fold increase in image size, the phosphor crystals must be small and densely packed to minimize granularity. However, for a monolayer structure, the screen thickness determines the resolution (Csorba, 1985). The final output of the image intensifier output conversion screen is on the order of 5×10^6 photons per second per square millimeter (Link *et al.*, 1989). Veiling glare is a radiometric degradation that shows up on the output conversion screen (Seibert, Nalcioğlu, and Roeck, 1984). Electron and photon scatter within the image intensifier tube contribute to a large-scale blurring effect. This is most pronounced when the object has adjacent regions of low and high X-ray transmission as for example in the case of step transition in thickness. This aberration

affects the low-frequency response of the tube and distorts the gray level response of the digitized image.

Flux Measurement of the X-ray Generator

Calibration of the Image Intensifier (II) is needed for the development of a model for real-time X-ray Imaging as explained in the next chapter. The main step in the calibration procedure is to obtain a measure of the flux or dosage generated by the X-ray generator at different kvp and currents.

The X-ray spectrum is a white spectrum. A typical plot of the spectrum using a NaI detector is shown in Figure 2.3. The spectrum shows the variation in the photon intensity at a particular kVp and current. A plot of the photon intensities for a particular current and time with different kVp shows an increase in the area under the curves with an increase in kVp (Figure 2.4). An increase in kVp results in an increase in the flux generated by the generator. The dosage or flux can be computed using the intensity variation.

To take care of the attenuation of the glass plate in front of the II, we use the well know Lambert's law according to which

$$I = I_o e^{-\mu_{silica} X}$$

where

I = transmitted beam intensity

I_o = incident beam intensity

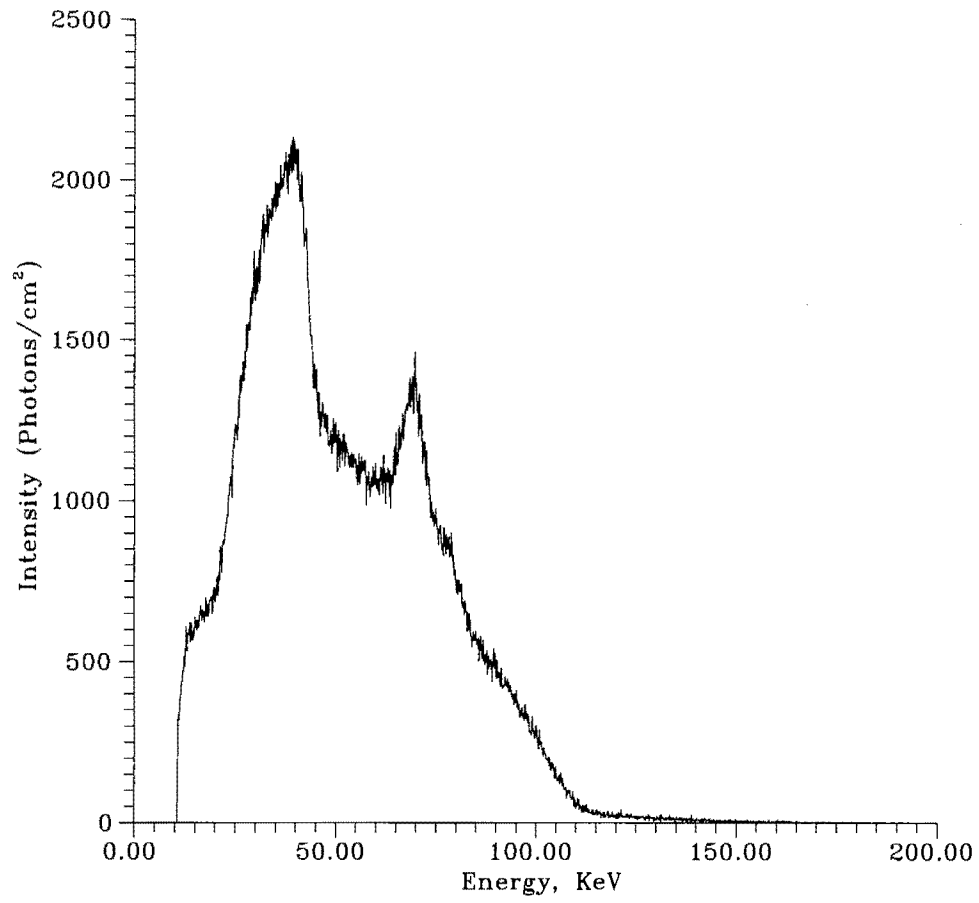


Figure 2.3: Plot of the spectrum from a NaI detector at 100 KeV, 0.01 mA

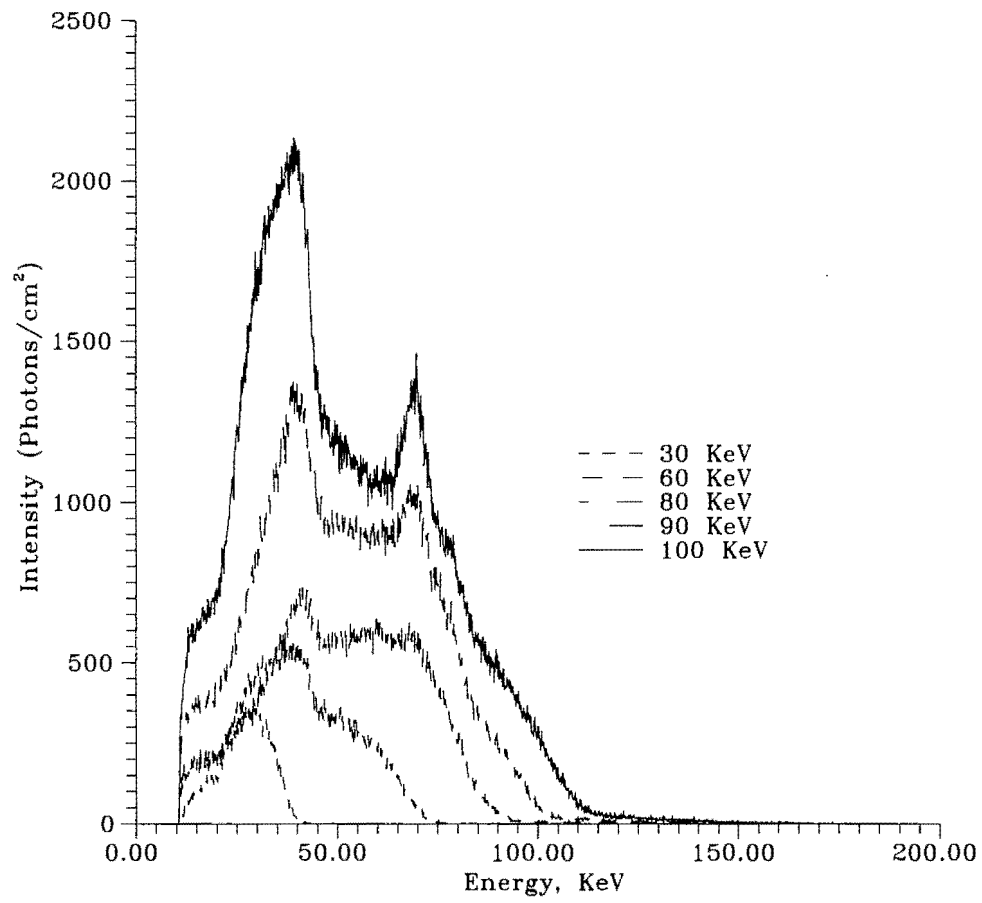


Figure 2.4: Plot of the spectra from a NaI detector at different KeV

X = thickness of the glass envelope
 in front of the Image Intensifier
 μ_{silica} = linear attenuation coefficient
 of silica.

Energy absorbed in one gm/cm² of air is given by

$$E (\mu_{en})_{air}$$

where

E = Energy
 $(\mu_{en})_{air}$ = coefficient which indicates the amount of energy
 deposited in one gram of air

Also note that 1 roengten deposits 87.7 ergs/gm in air. So in air

$$E (\mu_{en})_{air} = 87.7 R \text{ ergs/gm}$$

where

R = dosage in roentgens

Note that the units of $(\mu_{en})_{air}$ are cm²/gm. So

$$\frac{E}{R} = \frac{87.7}{(\mu_{en})_{air}}$$

Recall that the energy/cm² is $Ih\nu$ where $h\nu$ is the energy of one photon and there are I photons/cm². Consequently

$$Ih\nu/R = 87.7/(\mu_{en})_{air}$$

Converting the energy in ergs to MeV, we have

$$I/R = 87.7/1.6 \times 10^{-6} h\nu$$

and hence

$$R = (\mu_{en})_{air} h\nu I / 5.48 \times 10^7$$

In order to obtain the actual measure of dosage we should also take into consideration the finite size of the collimator and the radial divergence due to the differences in the positions of the image intensifier and the NaI detector. Therefore

$$R = C \times ((\mu_{en})_{air} h\nu I)$$

where

$$C = \frac{\pi a^2}{5.48 \times 10^7} \left(\frac{r_2^2}{r_1^2} \right)$$

$$\pi a^2 = \text{area of the collimator}$$

$$\frac{r_2^2}{r_1^2} = \text{radial divergence factor}$$

Now, for a white spectrum we have,

$$\sum_{E=0}^{E_{max}} R_E = C \times \sum_{E=0}^{E_{max}} (\mu_{en})_E h\nu_E I_E$$

This expression is used to compute the dosage using the photon intensity variation.

Calibration of Sodium Iodide Detector

The expression for flux or dosage of an X-ray generator, given the photon intensity variation was derived in the previous section. In order to measure the photon intensity variation, a discrete detector is required. A Sodium Iodide detector is used here for making the photon intensity measurements. The detector has to be calibrated before it can be used in a measurement procedure. Hence, a brief explanation about the detector and its calibration is given below.

The Sodium Iodide (NaI) detector is an inorganic detector that converts photon energy to visible light. The amount of light generated is proportional to the energy of the photons. A photomultiplier tube is coupled to the detector crystal to convert the weak light output into a corresponding electrical signal. The current pulse output of the photomultiplier tube is fed into a preamplifier that shapes the signal. An amplifier subsequently boosts the amplitude of the signal and provides a 0 to 10 volt pulse. The result is an energy sensitive detector response that can be gated using a multichannel analyzer (MCA). The digital detector is capable of registering the component of the signal that lies within a selected energy window filtering out the rest of the energy in a multienergetic beam (beam with a white spectrum).

As the spectrum is divided into different energy bins, a calibration procedure is required to determine the actual KeV of the photon the detector is sensing. To accomplish this isotope sources with known gamma intensity values are used. As these values are fixed, the energy bins corresponding to the particular KeV is noted. For different isotope sources, different energy bin values are noted. A plot between the energy bins and KeV gives the calibration curve for the detector. A typical calibration curve is shown in Figure 2.5.

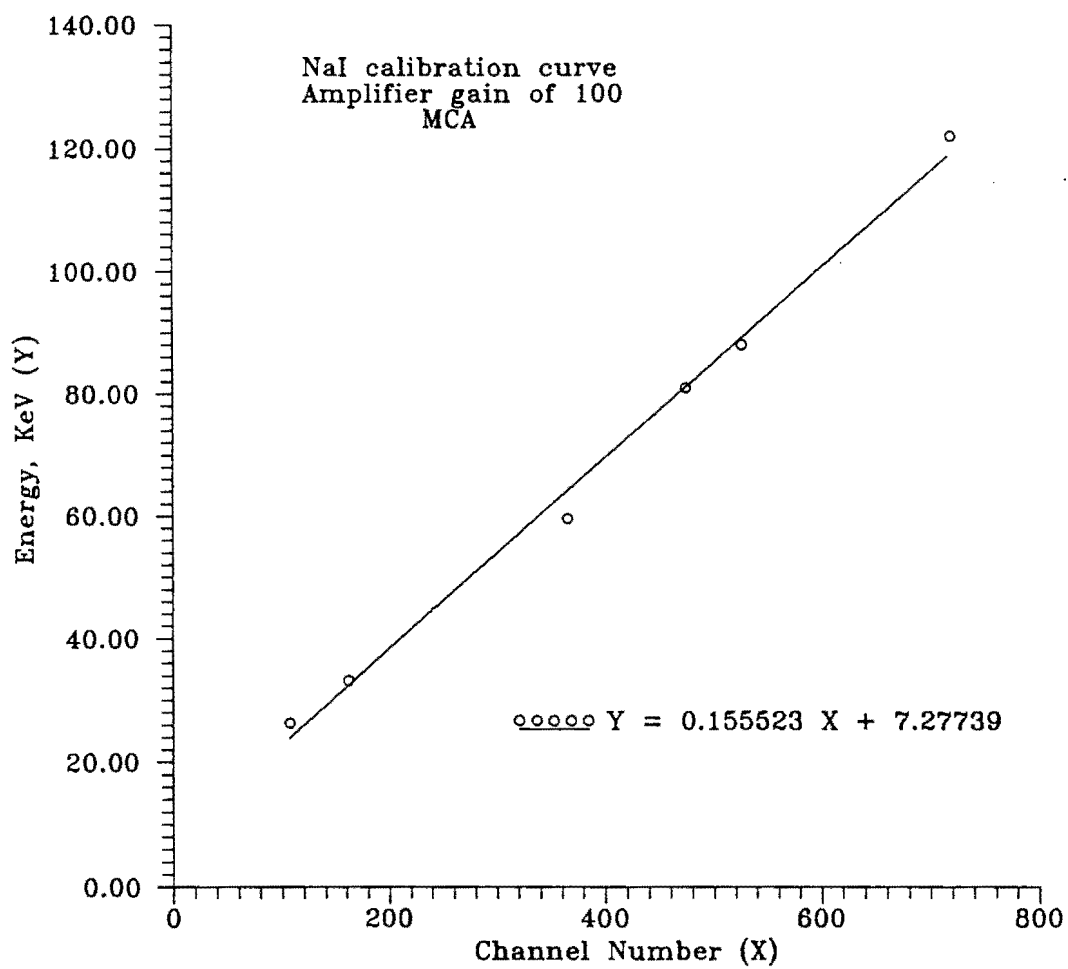


Figure 2.5: Calibration curve for the NaI detector

Calibration Plots for the X-ray II-TV System

A typical real-time X-ray system as used in industry is shown in Figure 2.6. In order to model the detector for the real-time X-ray system (II) we partition it into two systems, one containing just the generator and the image intensifier (Figure 2.7) while the other contains the imaging system (Figure 2.8).

The first step is to obtain a relation between the the generator flux and the light intensity at the output of the image intensifier. This can be done as follows. Spectra were obtained by keeping the kVp constant and varying the current. The procedure was then repeated for different kVp. The photon intensity variation in these spectra was then converted to dosage as explained earlier. At each current and kVp setting on the generator, the light intensity at the output of the II is measured using a photodiode. The diode converts the incident light into a corresponding voltage. A plot between the flux and the output voltage of the photodiode indicates the calibration of the X-ray - II system. A typical plot is as shown in Figure 2.9. Note the variation in the slope of the curves with a change in kVp. This indicates that the II is energy sensitive.

The next step is to obtain a relation between the output voltage of the photodiode and the gray scale output of the monitor. These calibration curves serve in modeling the imaging system consisting of the camera, frame grabber and the monitor. To perform this step a variable light source is used to produce different light intensities. LEDs of different colors were used as the varying light sources. The current through the LEDs was varied using a Digital to Analog converter to obtain different intensities. At each intensity of light the output voltage of the photodiode was measured, and digitized using an Analog to Digital converter. Again, by varying the current through

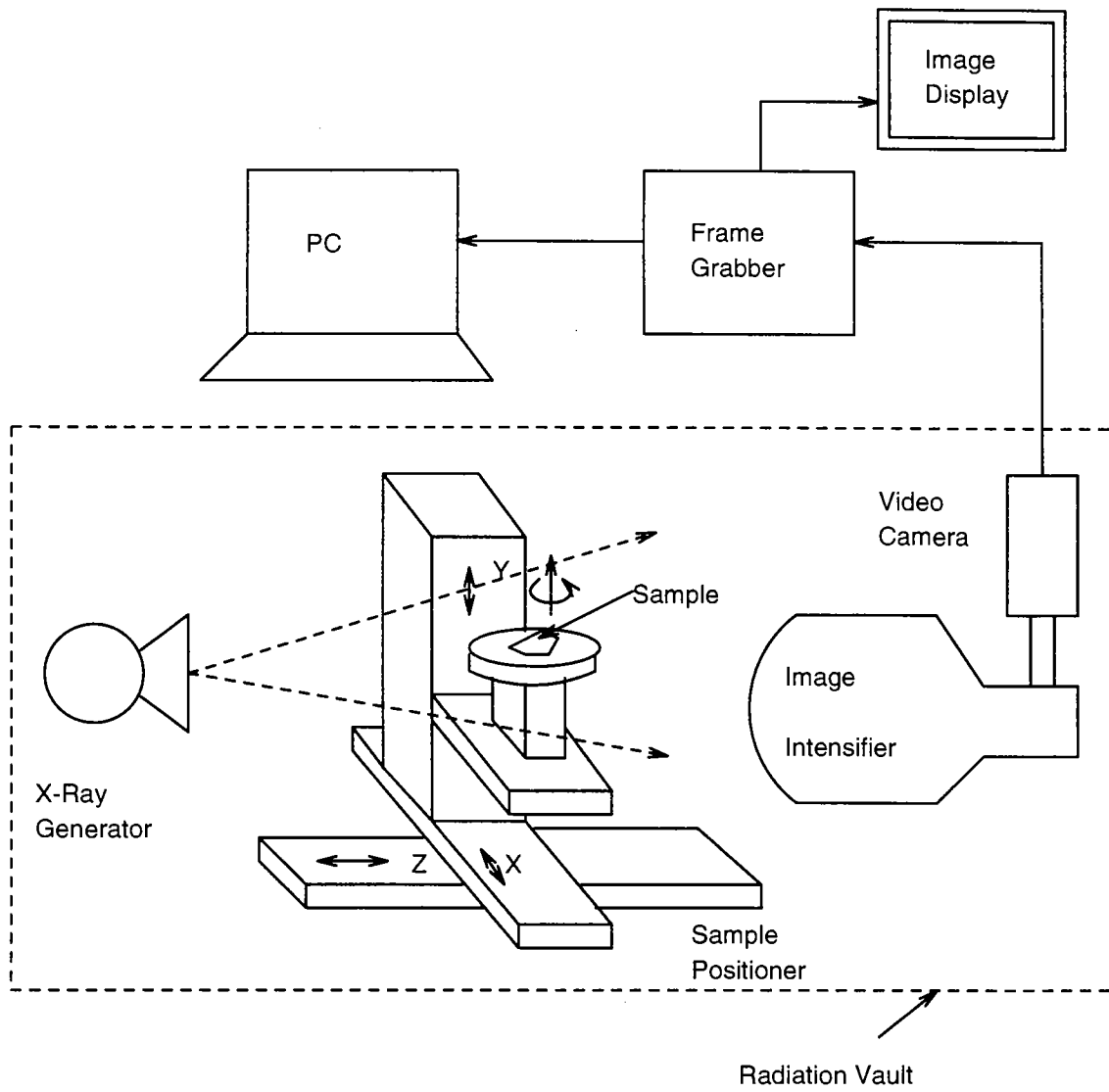


Figure 2.6: Real time X-ray system

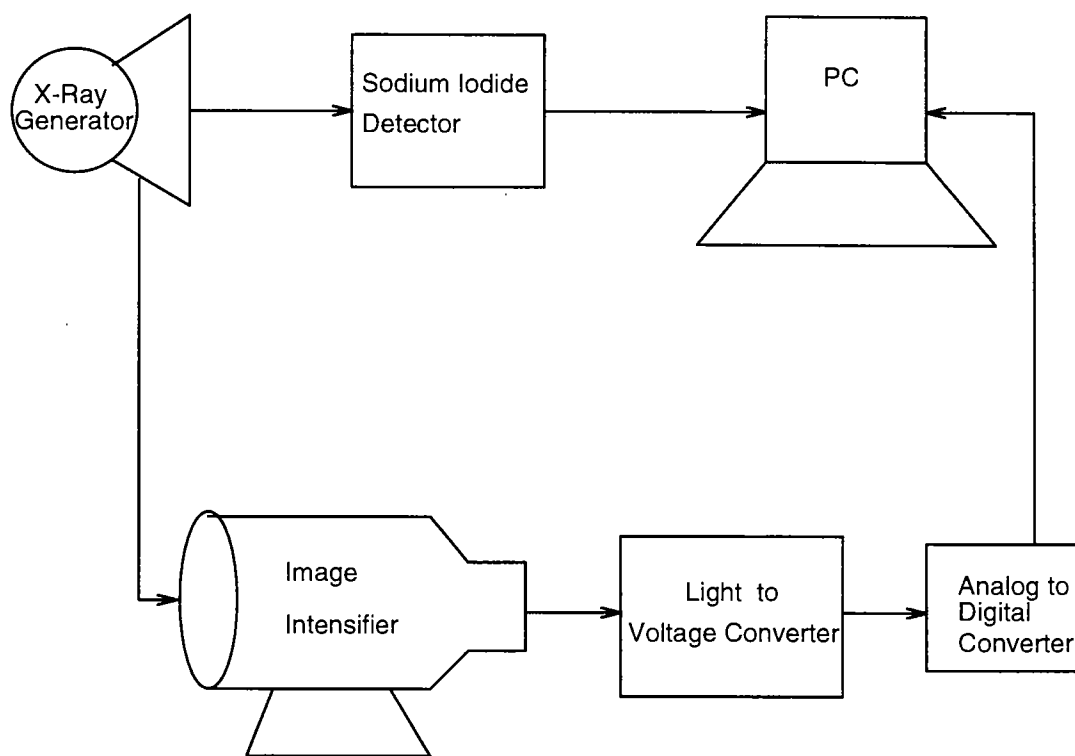


Figure 2.7: X-ray - Image Intensifier System

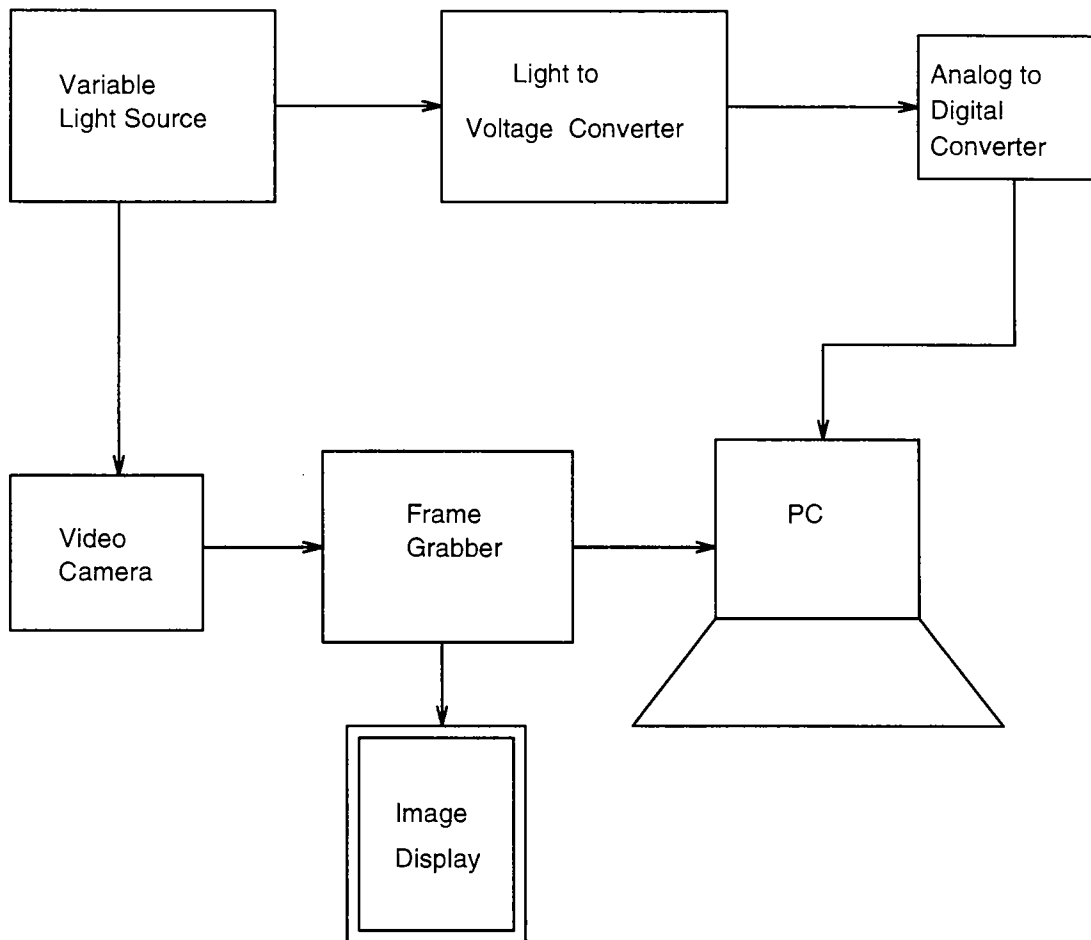


Figure 2.8: Imaging system

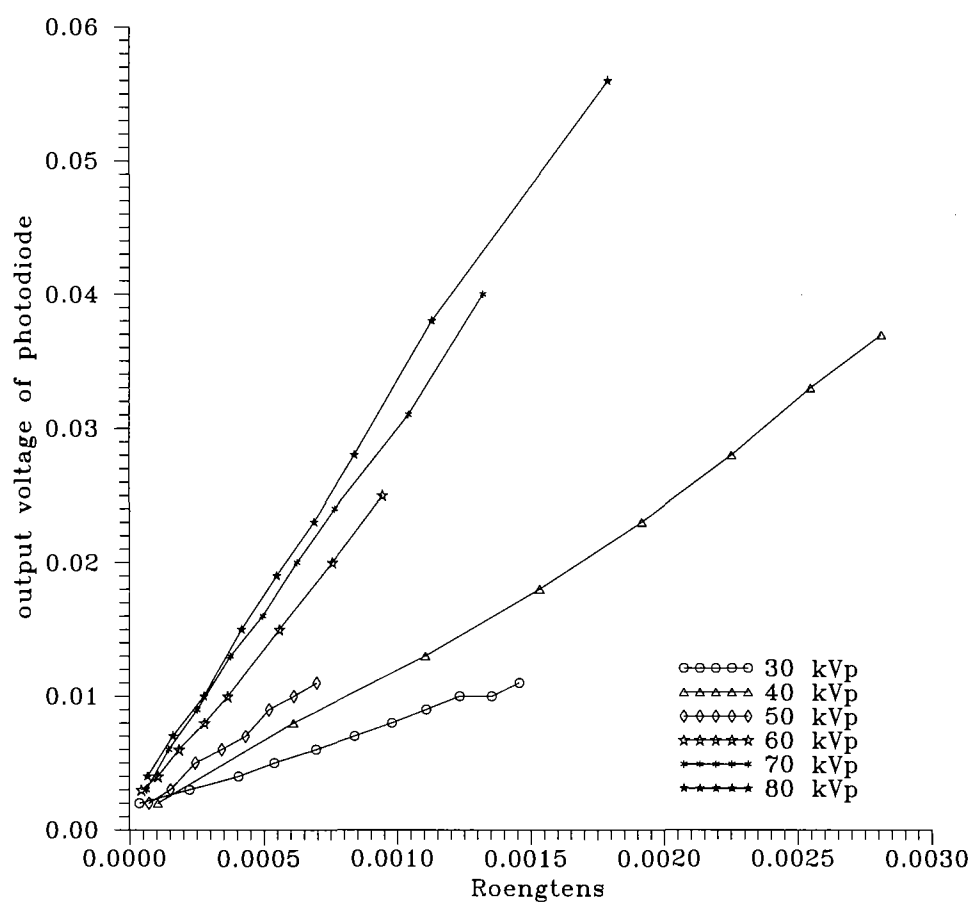


Figure 2.9: Calibration curves for the X-ray Image Intensifier

the LED to get the same intensity of light, the gray level value at the output is noted by averaging about 100 frames over a certain region of interest. A plot between the output voltage of the photodiode and the gray scale output provide the calibration curves for the imaging system. A typical calibration curve using a red LED for the Sony 8-bit CCD camera is shown in Figure 2.10. From the figure, it can be seen that the curve is linear over a small range of intensity values after which it saturates. The experiment as described earlier was then repeated for green and yellow LEDs as well as an incandescent lamp using the same camera. These curves are plotted as shown in Figure 2.11. Note the wide variation in the curves depending on the light source used. The reason for this is as follows. The spectral response curve for the photodiode shows that the diode is more sensitive at the red end of the spectrum than towards the green. Hence the slope of the curves decreases as the colors of the LEDs vary from green to red. Since the incandescent lamp output has a marked red or infra-red component it has a smaller slope when compared to the curves obtained with other LEDs. These curves suggest that care should be exercised in selecting the type of light source when the system is modeled. The Image Intensifier is basically sensitive to the blue-green region because of the type of phosphor used. Hence the calibration curve that has been obtained using the green LED is the best approximation for the model.

The same experiment was then repeated for a vidicon and a CID camera. The corresponding calibration plots are shown in Figures 2.12 and 2.13. A comparison of the curves obtained for a green LED for the three cameras is shown in Figure 2.14. Note the non-linearity of the vidicon camera and the large amount of light required to saturate the camera as compared to the other two cameras. Hence the type of

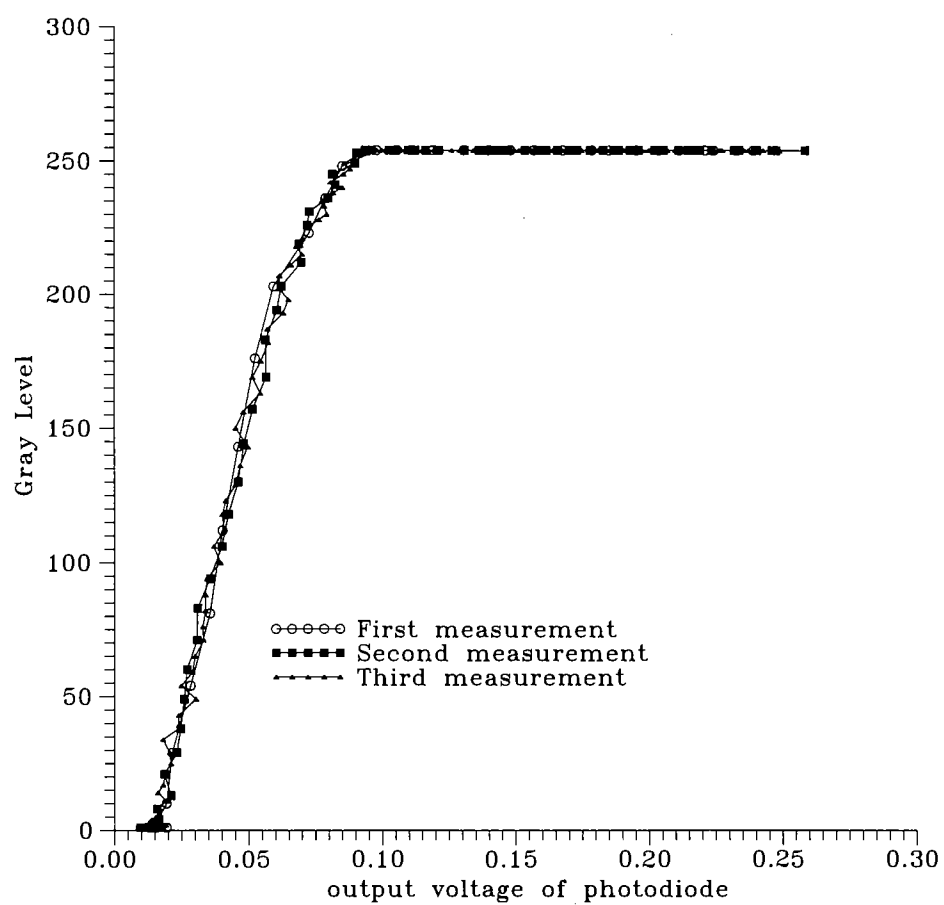


Figure 2.10: Calibration curves for the imaging system using the sony camera

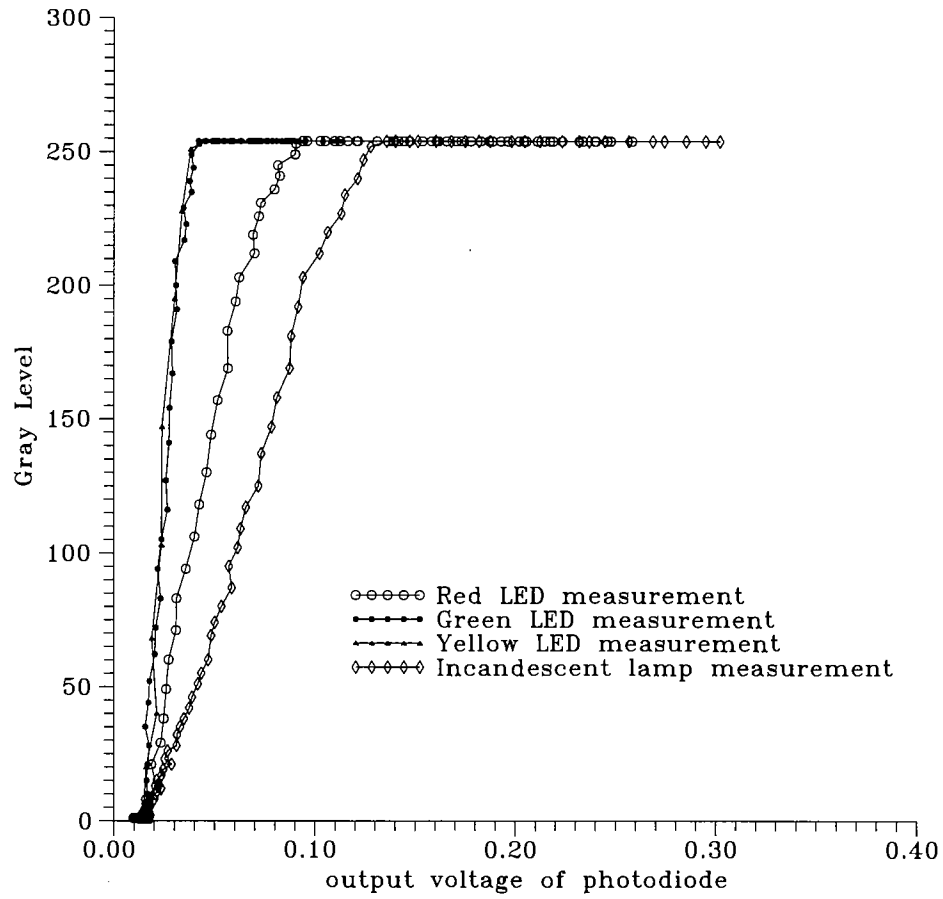


Figure 2.11: Calibration curves for the imaging system using red, green, yellow LEDs and an incandescent lamp for the sony camera

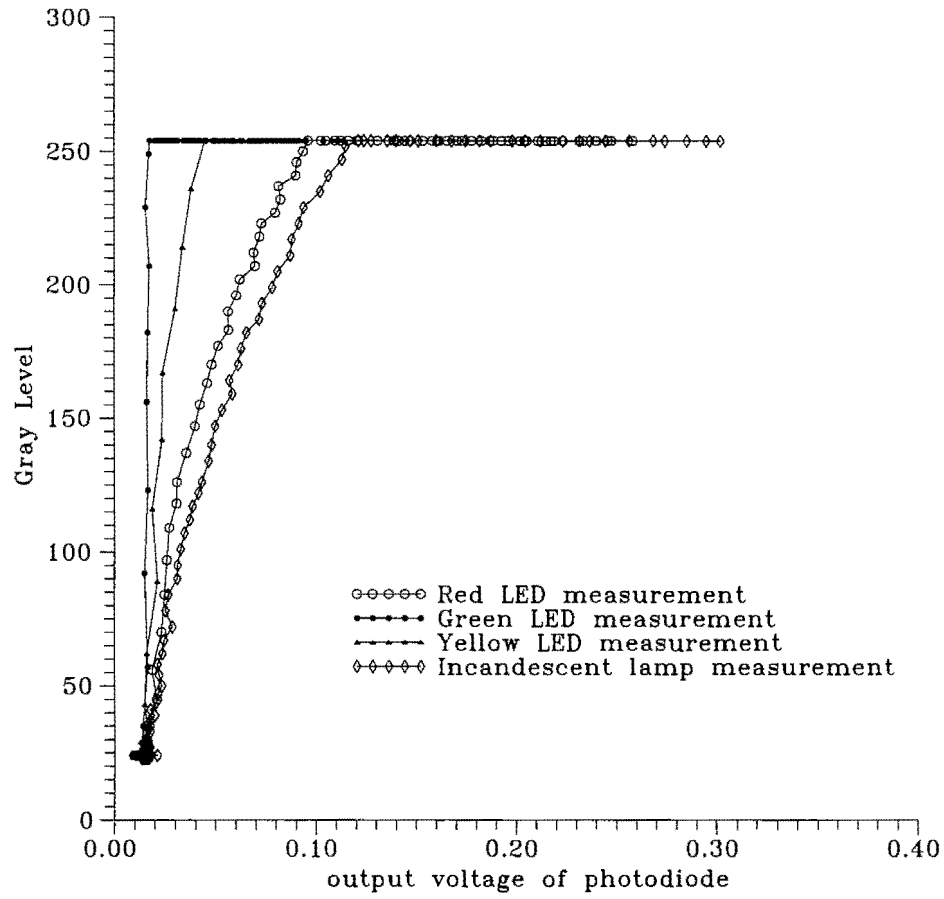


Figure 2.12: Calibration curves for the imaging system using red, green, yellow LEDs and an incandescent lamp for the vidicon camera

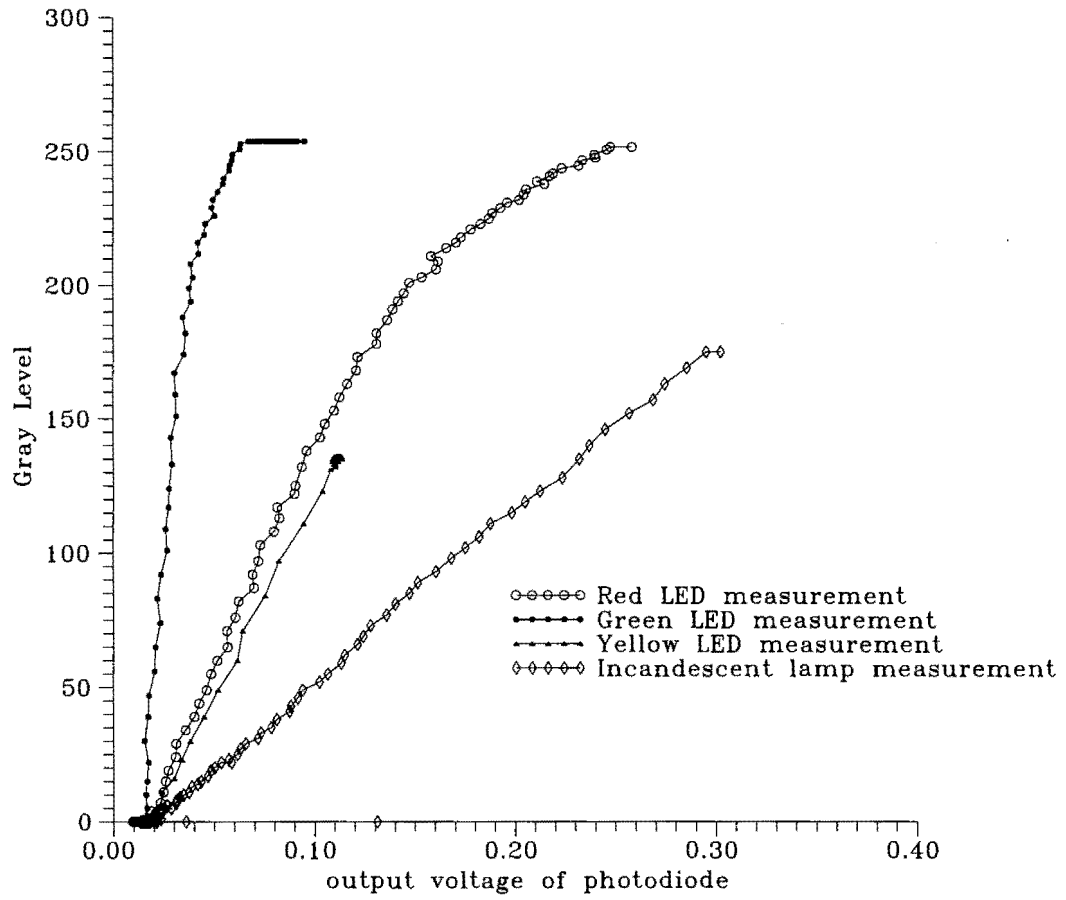


Figure 2.13: Calibration curves for the imaging system using red, green, yellow LEDs and an incandescent lamp for the CID camera

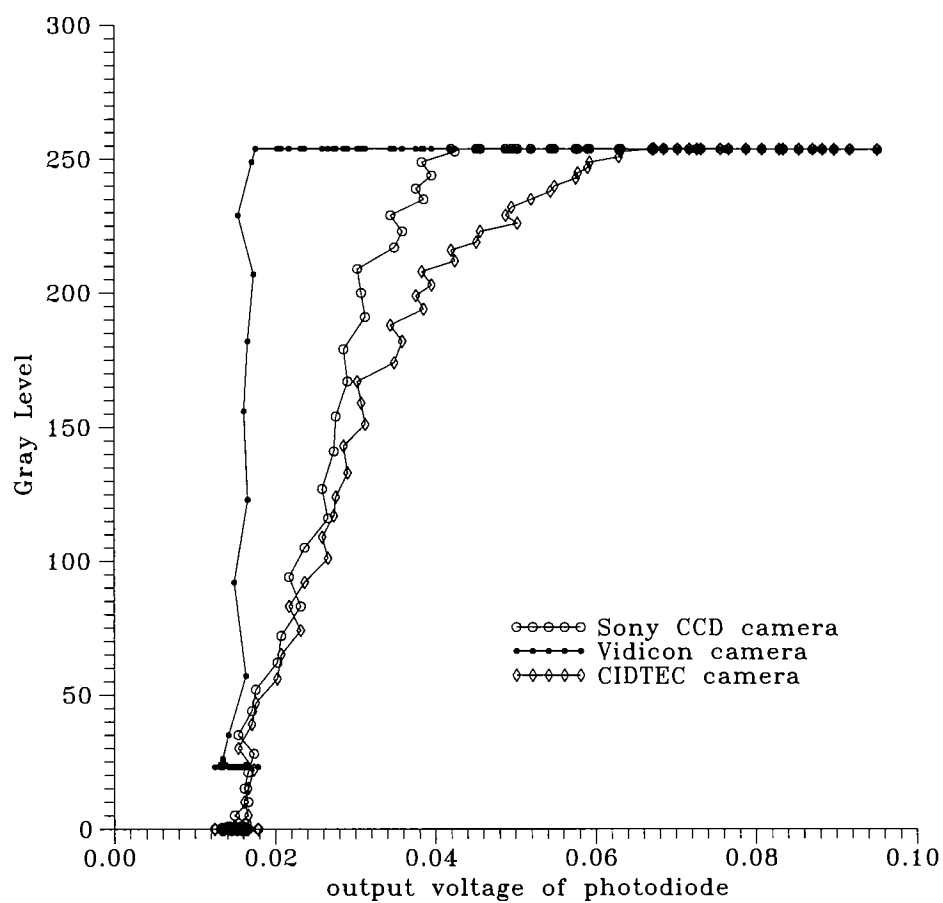


Figure 2.14: Calibration curves for the imaging system using different cameras for a green LED

camera also plays an important role in the accuracy of the modeling scheme.

Since, an 8-bit CCD camera is employed in the imaging system this has been used in the model. A linear fit was made to the curve as shown in figure 2.15. We, therefore, have two set of curves, one showing the relation between the flux of the generator and the output voltage of the photodiode while the other shows the relation between the output voltage of the photodiode and the gray scale output of the monitor. Using these two sets of curves, we can obtain a relation between the flux or dosage of the generator and the output gray level. Figure 2.16 shows a typical plot. Comparing this curve with the one obtained earlier only for the X-ray - II system reveals that though the image intensifier is capable of finer resolution we are limited due to the 8-bit digitization scheme associated with the CCD camera.

These curves represent the calibration of the detector in the real-time system. The process of incorporating these elements into the final model for the for the real-time X-ray system is explained in the next chapter.

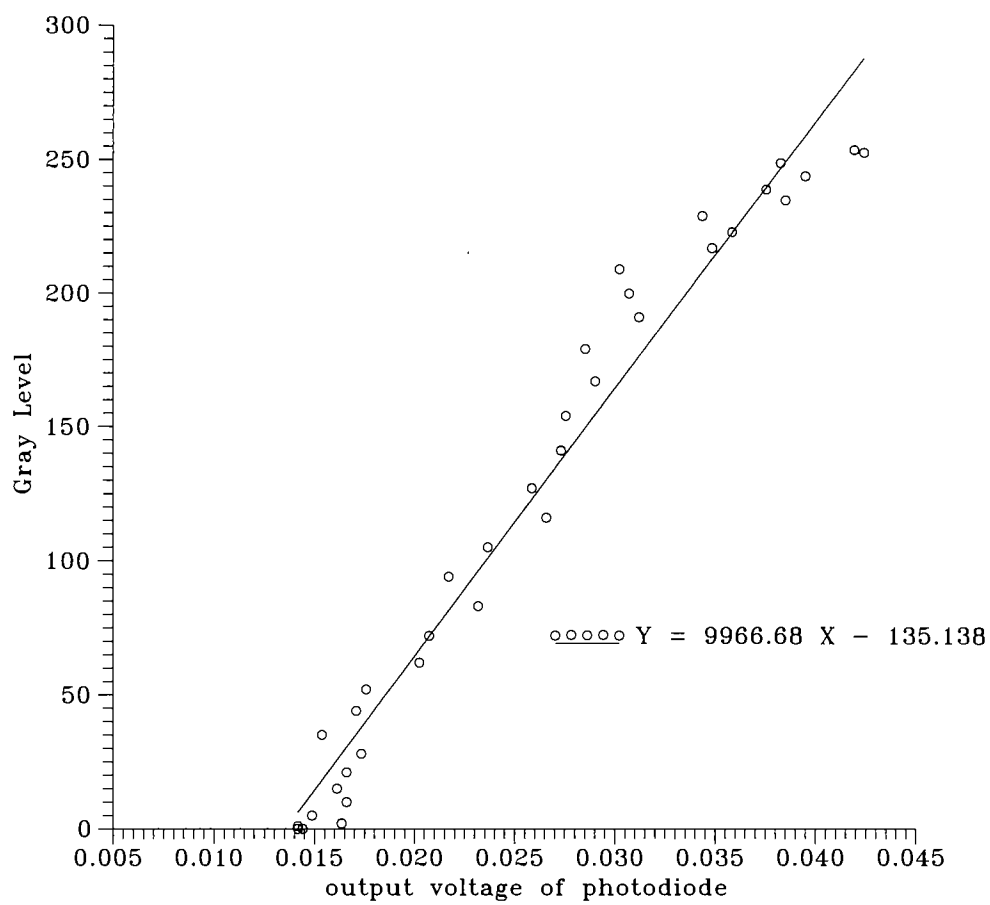


Figure 2.15: Calibration curve for the imaging system using the 8-bit CCD camera and the green LED

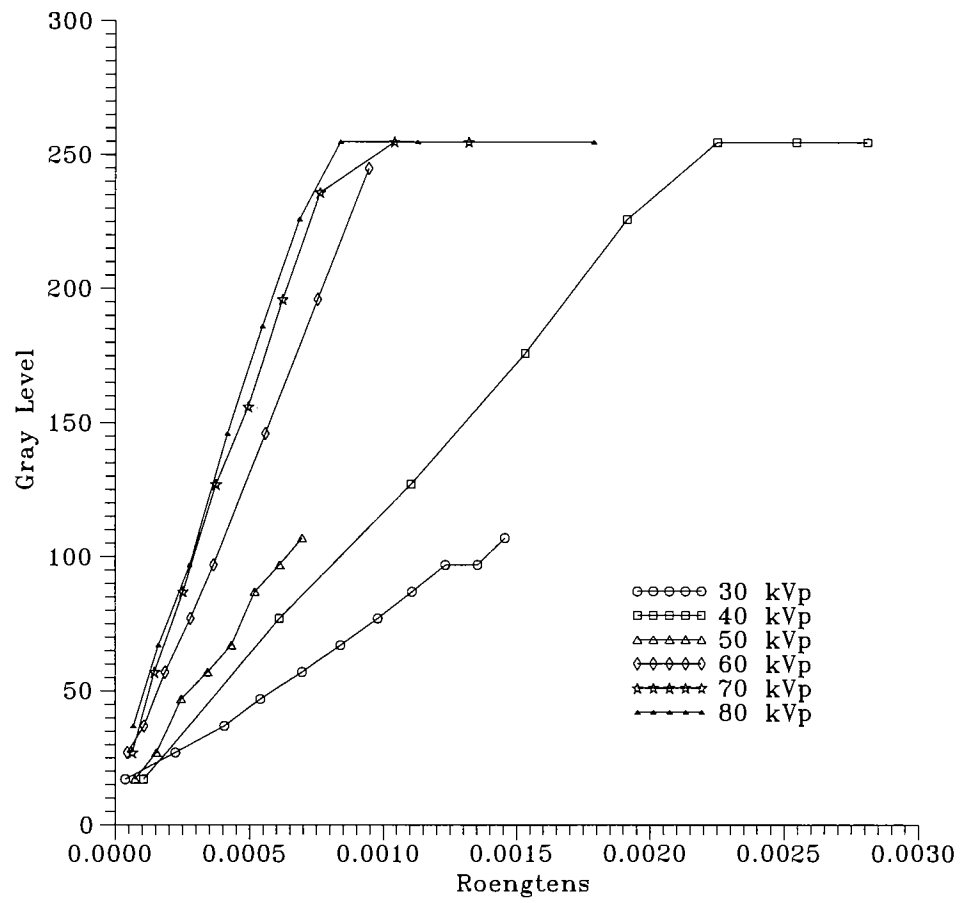


Figure 2.16: Calibration curves for the real time X-ray system

CHAPTER 3. A MODEL FOR REAL-TIME X-RAY IMAGING

Considerable work has been done by Gray (1988, 1989, 1990) in the area of x-ray simulation. Our aim here is to give a brief picture of the x-ray simulation model.

X-ray Simulation Fundamentals

The physics of the overall x-ray inspection process can be divided into three major independent models represented by the initial x-ray beam model, x-ray and target object interaction and x-ray and detector interaction models. Finally, a model is required for calculating the probability of detection or the figure of merit for assessing the inspectability of the part. A pictorial description of the simulation scheme is as shown in Figure 3.1.

Initial x-ray beam modeling

An important parameter in the initial x-ray beam modeling procedure is the x-ray energy spectrum. Since the interaction of x-rays with the target is energy dependent, the accurate initial x-ray beam computations are of vital importance. Initial x-ray beam calculations are based upon the electron-electron interaction cross sections (Lee, 1976). The angular dependence of the bremsstrahlung production is integrated over all angles. This simplification implies that the calculated intensities

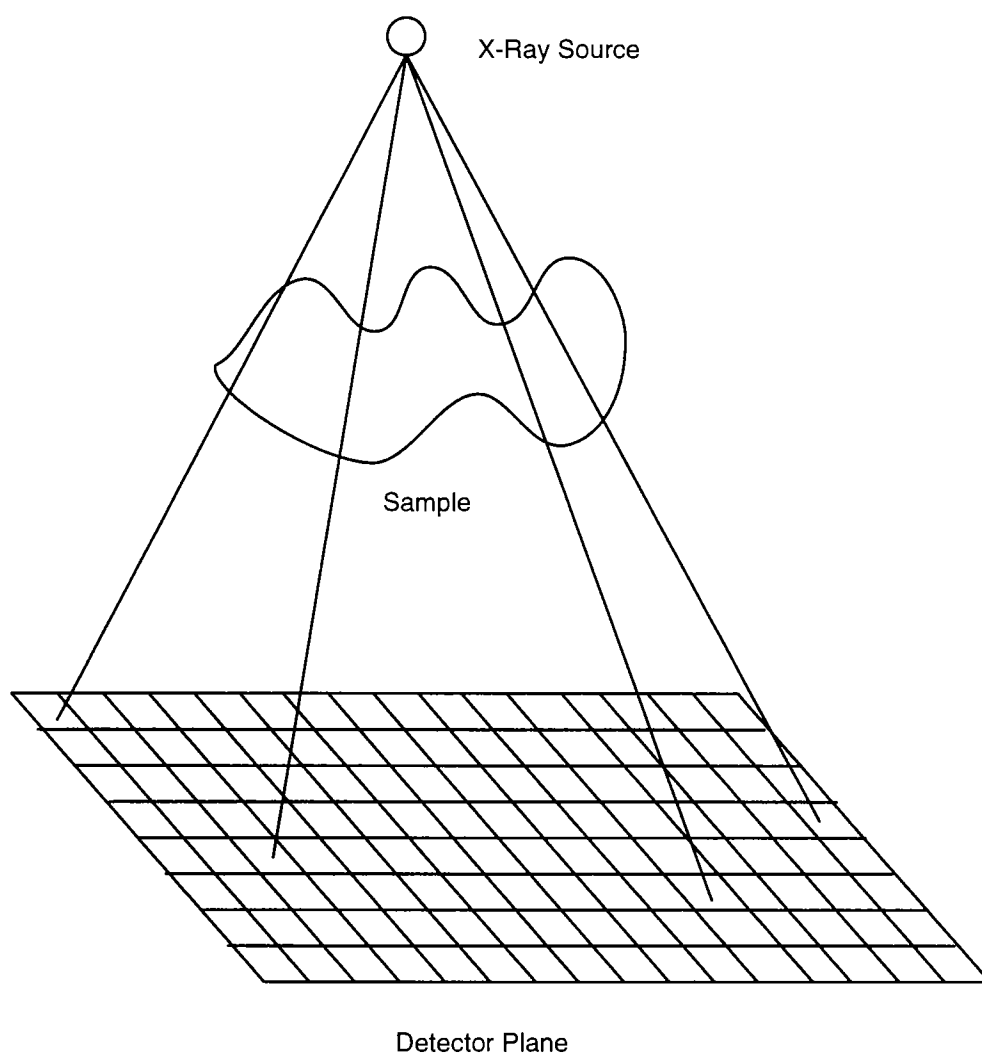


Figure 3.1: X-ray Simulation

will require a scaling factor to match the experimentally measured values. While the model takes the inherent filtering process into account, the calibration is most likely for the specific machine since in a sealed tube machine many parameters necessary for the calculations, for example, the angle of the target with the incident electron beam, cannot be adequately measured.

X-ray beam and target object interaction modeling

The conversion of the interaction cross sections depends on many assumptions. The most commonly used one is to assume that the target material is very dilute in the sense that the electron beam energy loss in the transverse of the material is negligible. This is clearly not the case for x-ray generators where all of the electron kinetic energy is lost in the material. Indeed, the heating of the target material is one of the major limitations on the production of high flux x-ray beams. The proper method for simulating the generation of the exiting x-ray beam for such generators is a monte carlo simulation wherein the multiple scattering of the electrons can be properly simulated or the solution to the diffusion transport equation of the system can be found. For more details please refer to (Gray, 1988). The sample is any object of arbitrary shape, whose composition can be selected from a variety of elements or simple compounds. A CAD package is used to design objects of complicated shape. The simulation tool is interfaced with SDRC-IDEas for obtaining the path lengths. Once the part shape database describing the designed part is ready, the path lengths are extracted from the database by an auxiliary program written in IDEas language. The resulting output file is used by the simulation program for computing the transmitted x-ray beam density.

A flaw in the shape of a truncated cone or an ellipse, also with a choice of materials, is positioned in the part. The position of the flaw can be independently altered in the x, y and z directions. The intensity at a point immediately above the detector plane is calculated by determining the photon flux from an elemental area on the source and then summing up all the contributions from the entire source. The attenuation of the x-ray beam is determined by calculating the coordinates of the x-ray path intersecting with the truncated cone or elliptic interface. X-ray beam hardening effects are calculated by utilizing the energy dependent absorption coefficients for the host and flaw materials. The energy dependent photon intensity at the plane immediately above the detector is given by

$$I(x, y, E) = I_o(E) \int_{area} \frac{e^{-\mu(E, x, y)\rho}}{r^2(x, y)} dA$$

where r is the radially divergent path x-ray length, ρ is the x-ray path length through the sample and μ is the energy dependent absorption coefficient of the sample. The integration is carried out over the finite extent of the elliptical source.

This photon distribution is then converted to a detector signal depending upon the detector sensitivity to the x-ray photon energy spectrum and intensity distribution. Using the calibration curves developed in the previous chapter the photon intensity can be converted into a corresponding gray level. Note that the image obtained here is one without any kind of distortion. A simulated image of a turbine blade using this model is shown in Figure 3.2.



Figure 3.2: Ideal x-ray image of the turbine blade

Modeling Pincushion Distortion

The next step in the development of the model is to add spatial distortion to the ideal image obtained in the previous section. The spatial distortion, caused by the curved input surface of the image intensifier is called pincushion distortion. An image warping method was used to model this spatial distortion. This procedure images a known object, say a grid of uniformly spaced holes in a plate, and fits a model to describe how the uniformly spaced features are distorted by the image intensifier to produce the measured image. The mapping is then applied to every pixel in the ideal image.

A procedure for pincushion distortion characterization by Doering (1992) is described. The objective here is to take an image of any object which has a specific geometry; a grid of uniformly spaced holes whose distances are known beforehand. It is then observed how these measurable features are distorted by the imaging system. So, a mapping function between the features of the object already know and the distorted image is obtained. This was done experimentally as explained below. A 10.5" by 10.5" piece of wire-wrap circuit board was used as the reference object. The board consists of a square array of 0.042 ± 0.005 " diameter holes on 0.1 ± 0.005 " centers. The board was affixed to the image intensifier input screen. The distorted hole positions of the grid were determined accurately by using an automatic procedure developed by Doering (1992). The thresholded pincushion distorted image of the grid is as shown in Figure 3.3. Note that the distortion is more pronounced at the edges than at the center of the image. Since, the correct hole positions are known because of the predefined geometry of the object, the correct and distorted hole positions are input to a polynomial curve fitting routine to determine the following mapping function.

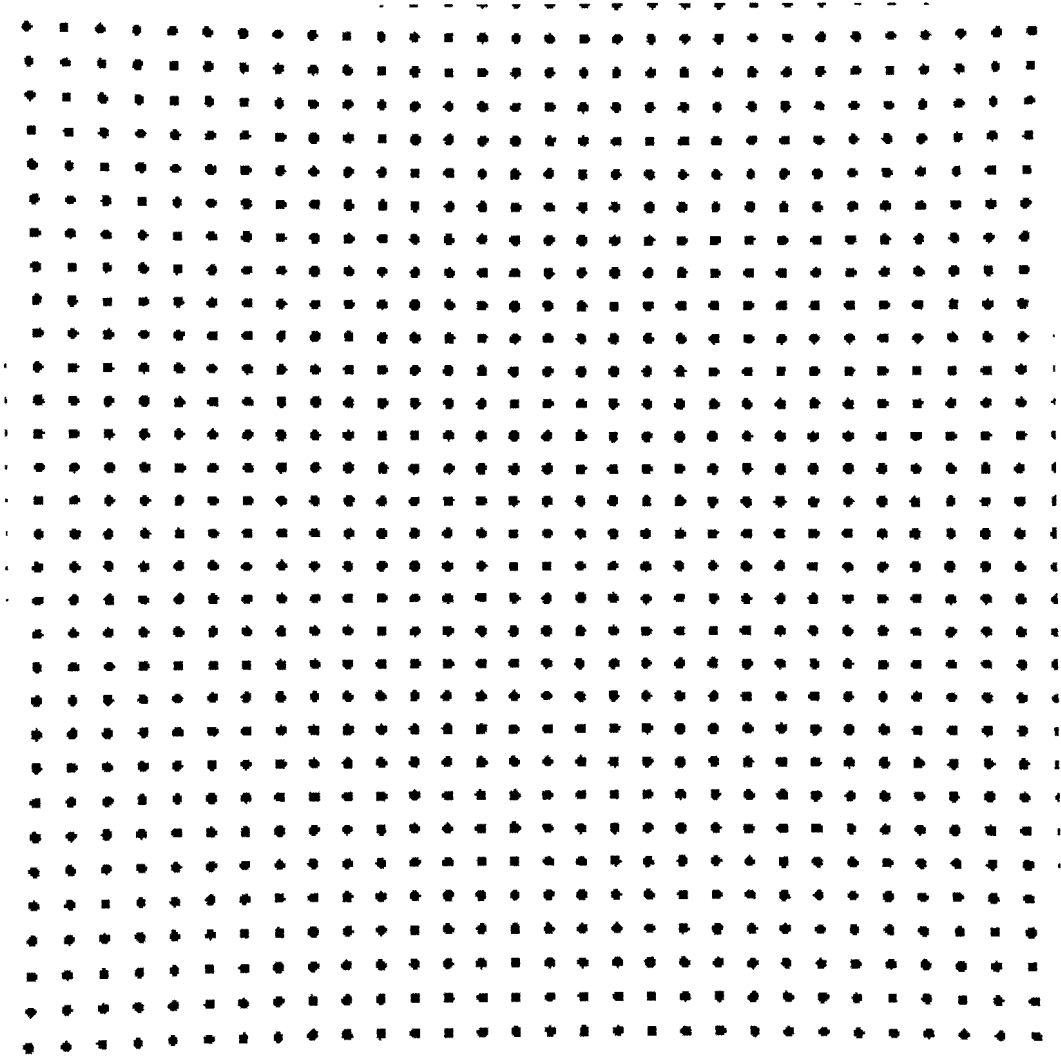


Figure 3.3: Thresholded pincushion distortion image

$$X_d = \sum_{i=0}^3 \sum_{j=0}^3 A_x(i, j) X_c^j Y_c^i$$

$$Y_d = \sum_{i=0}^3 \sum_{j=0}^3 A_y(i, j) X_c^j Y_c^i$$

where (X_d, Y_d) are the coordinates of the distorted hole positions, (X_c, Y_c) are the coordinates of the correct hole position, and A_x, A_y are 4×4 matrices of polynomial coefficients. Once the polynomial coefficients are known, the above mapping function can be applied to every pixel in the ideal image. A simulated image of the turbine blade which is spatially distorted is as shown in Figure 3.4.

Incorporation of Blur

The blurring in a real-time x-ray system is a combination of two factors, one is the phosphor bloom of the image intensifier and the other is caused by the blur introduced due to the camera in the imaging chain. To characterize the blur of the real-time system, the impulse response of the imaging system also known as the Point Spread Function (PSF) has to be determined. A method is described here to measure the PSF of the system.

The point spread function describes the impulse response of the optical system. The modulation transfer function (MTF) is the magnitude of the Fourier transform of the point spread function and measures the frequency response of the optical system. It is practically impossible to generate an impulse function. For example, to create an impulse function for the image intensifier, it means that a large number of x-ray photons are to be collimated in an extremely small beam. Traditionally, optical knife edges have been used to measure the MTF of optical lenses and CCD arrays. The

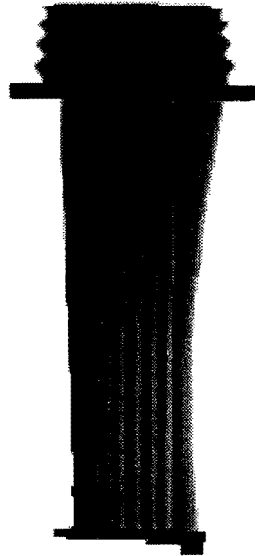


Figure 3.4: Pincushion distorted x-ray image of the turbine blade

knife edge serves as a step function to the optical lens. Differentiating this response gives the PSF of the system. A similar approach can be used for characterizing the PSF of the real-time x-ray system. A lead plate can serve as the knife edge in this case. Obviously, there is some amount of noise in the measurement procedure and this noise is further enhanced when the step function response is numerically differentiated to get the impulse function response. But, the main drawback of this method is the undersampling in the edge transition region where only 5 to 10 pixel values are available to characterize the edge (Doering, Gray and Basart, 1992). So a different technique developed by Glasser, Valliant and Chazallet (1988), where the output of a single pixel is monitored while the knife-edge is shifted in sub-pixel increments, was implemented.

The experimental procedure is explained below. The lead plate was mounted on the sample positioner and placed at such a position from the image intensifier so that 1:1 magnification was achieved. The edge of the plate was aligned with the central axis of the x-ray source to minimize the blurring due to geometrical unsharpness. The plate is stepped in $5\mu\text{m}$ increments and at each position 100 frames are averaged. The total scan length is taken to include enough measurements in the edge transition region. This scan was then numerically differentiated using the forward difference approach i.e., $y(n) = x(n + 1) - x(n)$. The scan was then smoothed to reduce the noise and a gaussian fit was made. A typical scan is shown in Figure 3.5. The full-width-at-half-maximum from the gaussian fitted curve is then measured (FWHM; $\text{FWHM} = 2.354$ times the standard deviation of the Gaussian function). Note that the Gaussian follows the smoothed derivative in Figure 3.5 very well. This is expected since the combined PSFs of the many separate components in the imaging chain tend

to a Gaussian due to central limit effects (Andrews and Hunt, 1977).

From the FWHM of the Gaussian its standard deviation can be found. Using this value of the standard deviation, a 2-D Gaussian function can be generated. The 2-D Gaussian function represents the PSF of the system. We use the PSF in the image restoration routines that are described in the next chapter.

Once the blurring function is determined, the image at the output plane are given by the expression (2-D convolution)

$$y[m][n] = x[m][n] * h[m][n]$$

where x is the ideal image, y is the blurred image and h is the point spread function of the system. A simulated image of the turbine blade now which is blurred is shown in Figure 3.6.

Addition of Noise

The noise properties of most communications systems involve additive noise only. The energy per photon, $h\nu$, in these lower-frequency spectra is relatively small, so that copious amounts of photons are available for the weakest signals being considered. Thus the uncertainties lie almost completely in the noise added by the measurement system rather than those of the signal itself. Quantum noise, which is the primary source of noise in x-ray systems, is introduced due to the quantization of the energy into photons each having an energy $h\nu$. This quantum noise is Poisson distributed.

The emission of photons from the x-ray source is a Poisson process (Parzen,

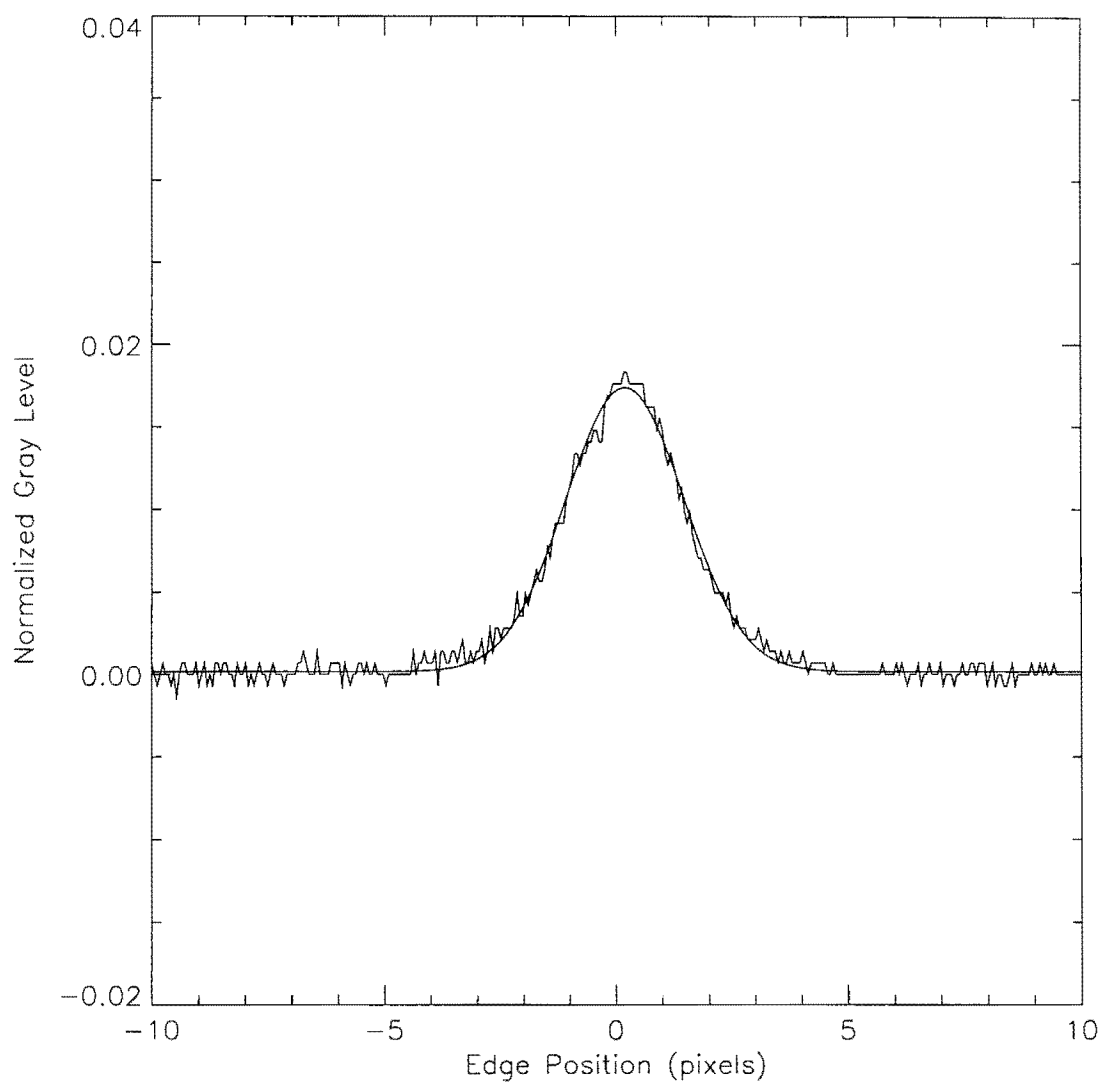


Figure 3.5: Numerical derivative of smoothed edge scan data (noise-like signal), with overplot of fitted Gaussian (smooth signal)

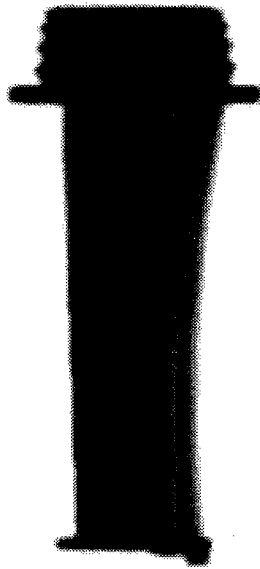


Figure 3.6: Blurred x-ray image of the turbine blade

1960) whose probability density is given as

$$P_k = \frac{\lambda^k e^{-\lambda}}{k!}$$

where P_k is the probability of emitting k photons, in a given time interval, and λ is the average number of photons emitted in that interval. For each pixel in the image, a random number is drawn from a Poisson distribution that depends on the pixel value of the input image is generated to produce the output image (Press et al, 1988).

A blurred, noisy and pincushion distorted version of the image of the turbine blade is shown in Figure 3.7. A real-time image obtained by frame-averaging 10 frames is as shown in the figure 3.8. Comparison of these two images visually shows a high degree of correspondence between the two images. A quantitative comparison cannot be done effectively due to image registration problems and problems associated with the CAD model generated for the images.

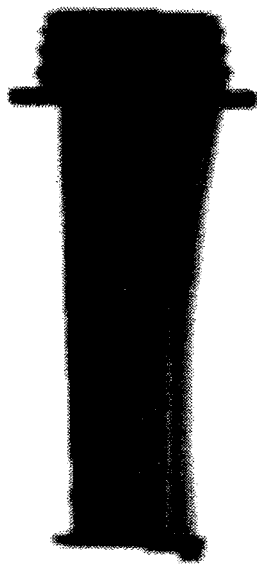


Figure 3.7: Blurred, pincushion distorted and noisy x-ray image of the turbine blade

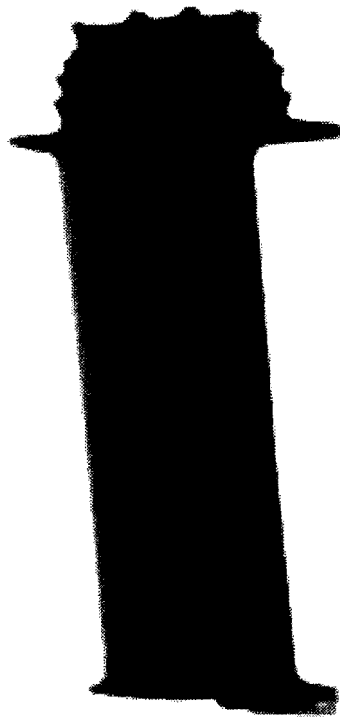


Figure 3.8: Real time x-ray image of the turbine blade

CHAPTER 4. IMAGE RESTORATION

In X-ray NDE we either use film or real-time detectors. Film has the advantages of high resolution and excellent dynamic range, but it cannot be used for real-time applications. Real-time detectors (image intensifiers) allow the X-ray field to be viewed continuously but this advantage is offset by its lower resolution and poorer dynamic range compared to film. The purpose of image restoration here is to improve the contrast and spatial resolution of real-time detectors. In image intensifier based real time X-ray NDE systems we are concerned with two types of degradations; one is due to the inherent phosphor bloom of the image intensifier while the other is due to the camera MTF. A procedure to measure the PSF of the system was explained in the previous chapter and this will be used in our restoration algorithms. Various linear and non-linear deconvolution techniques are discussed and compared with respect to their effectiveness in the restoration of X-ray images.

Preliminaries

Any image acquired by optical, electro-optical or electronic means is likely to be degraded by the sensing environment. The degradations may be in the form of sensor noise, blur due to camera misfocus, relative object-camera motion, and so on. Image restoration is concerned with filtering the observed image to minimize the

effect of degradations. The effectiveness of image restoration filters depend on the extent and the accuracy of the knowledge of the degradation process as well as on the filter design criterion. Image restoration differs from image enhancement in that the latter is concerned with accentuation or extraction of certain image characteristics without taking into account the actual process of degradations. Image restoration schemes are based on a precise understanding of the underlying physical process, whereas enhancement schemes are often adhoc. Consequently, restoration techniques often depend only on the class or ensemble properties of a data set, whereas image enhancement techniques are much more image dependent.

A typical imaging system consists of an image formation system, a detector, and a recorder. For example, in x-ray imaging, the x-ray source focuses an image on the image intensifier, which is scanned for transmission or recording of the image by a CCD camera. A general model for such systems, assuming the system to be linear shift invariant, can be expressed as

$$y(m, n) = \sum_{k=0}^{N-1} \sum_{l=0}^{N-1} h(m-k, n-l)x(k, l) + \eta(m, n)$$

where,

$y(m, n)$ = output degraded image

$x(m, n)$ = input ideal image

$h(m, n)$ = point spread function of the system

$\eta(m, n)$ = discrete white noise field

$m, n = 0 \dots N-1$

For a real-time X-ray imaging system, $y(m, n)$ is the image obtained after the digitization of the field at the output phosphor of the image intensifier; $h(m, n)$ models the phosphor bloom of the image intensifier and the camera MTF; $\eta(m, n)$ is the white noise field (it does not take care of the noise due to photon counting statistics, which is Poisson in nature). The point spread function is often represented differently in the different restoration algorithms to facilitate ease of representation. In matrix notation the PSF is usually represented as H or C_{ij} while the Fourier transform of the PSF is often represented as $H(\omega_1, \omega_2)$

The aim of the various deconvolution techniques is to reduce the mean square error between the ideal and processed images. For x-ray imaging in addition to the white noise there is a signal dependent noise which is Poisson in nature. This noise is multiplicative in nature. Some of the non-linear deconvolution techniques such as the maximum entropy method (MEM), perform better in such cases. These techniques are discussed in the next section.

Different Restoration Filters

In this section we will look into various techniques for the restoration of x-ray NDE images.

Pseudo inverse filter

Inverse filtering is the most intuitive technique for image restoration. It is the process of recovering the input of a system from its output. Inverse filters are useful for precorrecting an input signal in anticipation of the degradation caused by the system, such as correcting the nonlinearity of a display. The design of physically

realizable inverse filters is difficult because they are often unstable. For example for spatially invariant systems we can write,

$$\sum_{k=0}^{N-1} \sum_{l=0}^{N-1} h^I(m-k, n-l)h(k, l) = \delta(m, n), \quad \forall(m, n)$$

where $h(m, n)$ is the system transfer function of the degraded image. $h^I(m, n)$ is the inverse filter function and $\delta(m, n)$ is the unit impulse response.

If we compute the Fourier transform of both sides, we obtain $H^I(\omega_1, \omega_2)H(\omega_1, \omega_2) = 1$, or,

$$H^I(\omega_1, \omega_2) = \frac{1}{H(\omega_1, \omega_2)}$$

i.e., the inverse filter frequency response is the reciprocal of the frequency response of the given system. However, $H^I(\omega_1, \omega_2)$ is singular if $H(\omega_1, \omega_2)$ is a non minimum phase system i.e., it has zeros in the left half plane.

The pseudoinverse filter is a stabilized version of the inverse filter. For a linear shift invariant system with frequency response $H(\omega_1, \omega_2)$, the pseudoinverse filter is defined as

$$H^-(\omega_1, \omega_2) = \frac{1}{H(\omega_1, \omega_2)}, \quad H \neq 0$$

$$0, \quad H = 0$$

Here, $H^-(\omega_1, \omega_2)$ is also called the generalized inverse of $H(\omega_1, \omega_2)$, in analogy with the definition of the generalized inverse of matrices. In practice, $H^-(\omega_1, \omega_2)$ is set to zero whenever $|H|$ is less than a suitably chosen positive quantity ϵ . It can be seen from the equation for an inverse filter that the filter is very sensitive to noise and even if the noise is small implementing this filter results in the amplification of noise.

Two different images were taken to verify the effectiveness of such restoration algorithms. One is a simulated image containing two objects which have very sharp edges. This image is then blurred with a 2-D gaussian with a variance of 1.3. The original image and a slice across the image are shown in Figures 4.1 and 4.2 respectively. The sharpness of the edges improve as different filters are applied to this image. The blurred and the inverse filtered images and the slices across these images are shown in Figures 4.3 and 4.4.

The other is a real-time image (100 frames used for frame averaging) of a resolution gauge. The resolution gauge is a square-wave pattern of alternating X-ray transparent regions increasing continuously in frequency from 1 to 10 lp/mm. The gauge is placed in contact with the input screen of the image intensifier and digitized using the same experimental setup that is used to measure the PSF. A 256×256 subimage was extracted for restoration and is shown in the Figure 4.5. The blurring of the image intensifier is evident in the letters, tic marks, and square wave pattern, that is visible to about 2.3 lp/mm. The result using the pseudo-inverse filter and a comparison of the slices across these images are shown in Figures 4.6 and 4.7.

Wiener filter

The main limitation of inverse and pseudoinverse filtering is that these filters remain very sensitive to noise. Wiener filtering is a method of restoring images in the presence of blur as well as noise.

Let $u(m, n)$ and $v(m, n)$ be arbitrary zero mean, random sequences. It is desired to obtain an estimate, $\hat{u}(m, n)$, of $u(m, n)$ from $v(m, n)$ such that the mean square

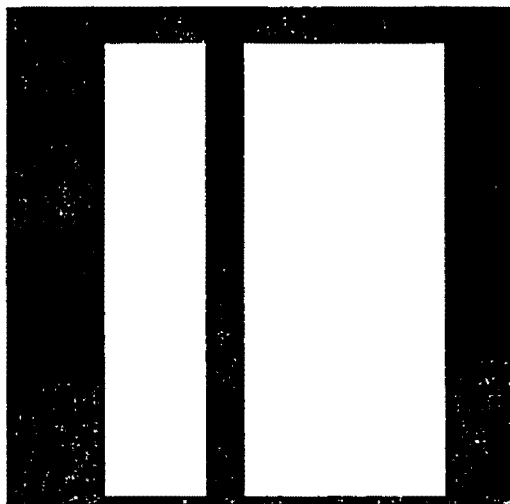


Figure 4.1: Ideal Image

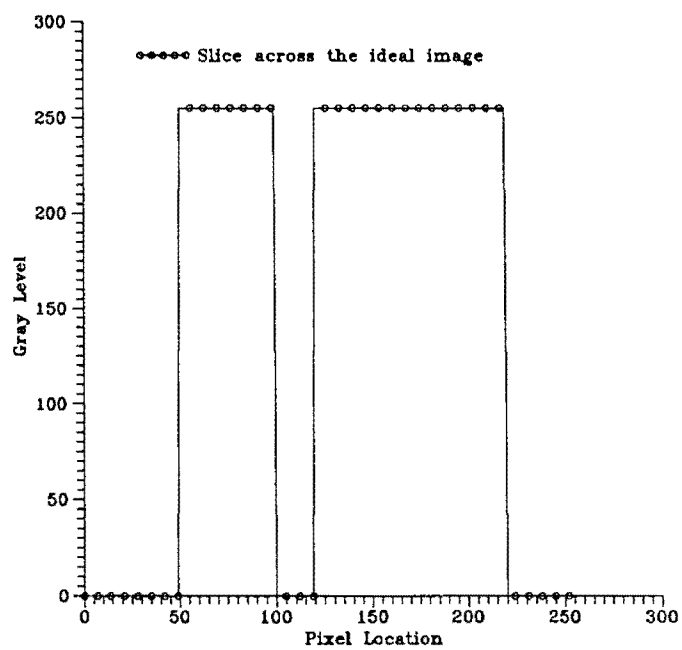


Figure 4.2: Slice across the Ideal Image

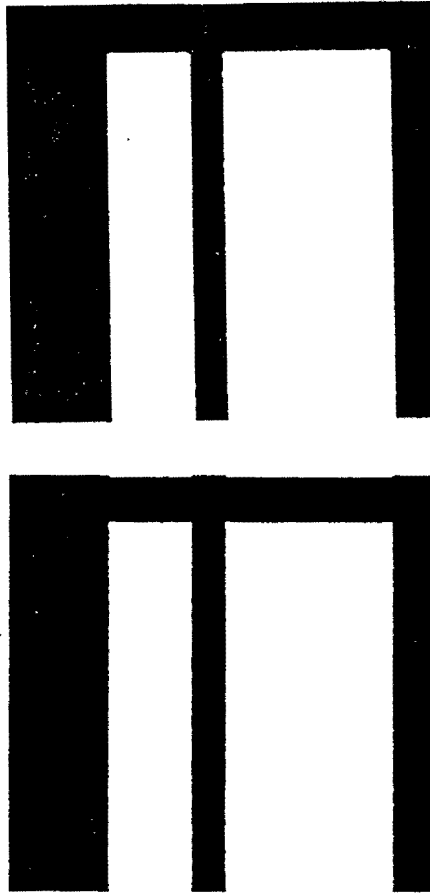


Figure 4.3: Blurred and pseudo-inverse filtered images

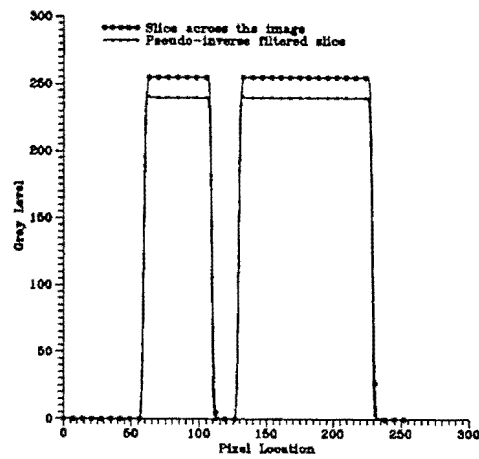


Figure 4.4: Input and Pseudo-inverse processed slice profiles

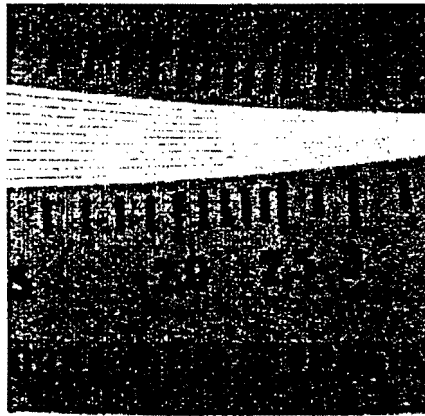


Figure 4.5: Real-time image of a resolution gauge

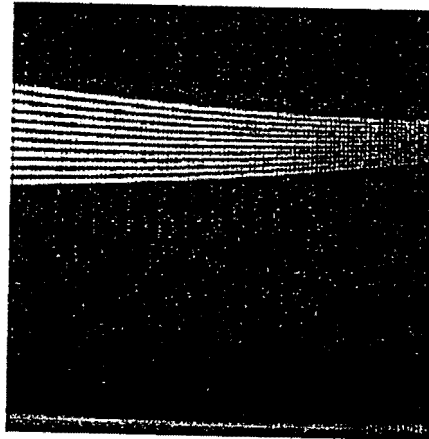


Figure 4.6: Pseudo-inverse filtered images of the resolution gauge

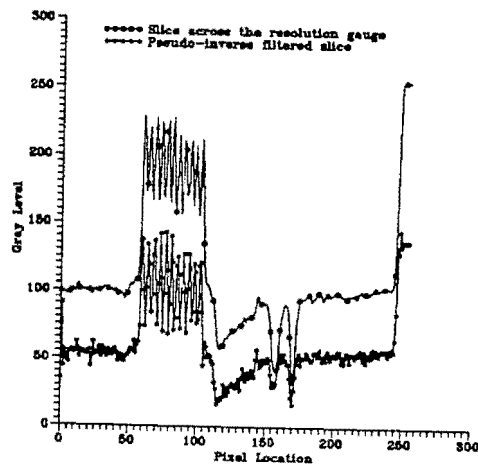


Figure 4.7: Input and Pseudo-inverse processed slice profiles of the resolution gauge

error

$$\sigma_e^2 = E[u(m, n) - \hat{u}(m, n)]^2$$

is minimized. This criteria is used to design a Wiener filter.

Thus for zero mean images the Wiener filter can be expressed as (Jain.. 1989)

$$G(\omega_1, \omega_2) = \frac{H^*(\omega_1, \omega_2)S_{uu}(\omega_1, \omega_2)}{|H(\omega_1, \omega_2)|^2 S_{uu}(\omega_1, \omega_2) + S_{\eta\eta}(\omega_1, \omega_2)}$$

where,

$G(\omega_1, \omega_2)$ = wiener filter coefficients

$H(\omega_1, \omega_2)$ = system transfer function

$S_{uu}(\omega_1, \omega_2)$ = power spectral density of the original image

$S_{\eta\eta}(\omega_1, \omega_2)$ = power spectral density of the noise

Since there is little information with regard to the original image or the noise variance, the above equation can be rewritten in a way that excludes these two quantities from the above equation. We then have

$$G(\omega_1, \omega_2) = \frac{H^*(\omega_1, \omega_2)}{|H(\omega_1, \omega_2)|^2 + 1/k}$$

where, $k = S_{uu}(\omega_1, \omega_2)/S_{\eta\eta}(\omega_1, \omega_2)$ is the SNR of the image.

The results obtained using this filter are shown in Figures 4.8 and 4.9 for the simulated image and 4.10 and 4.11 for the resolution gauge.

Iterative Wiener filter

A significant amount of prior knowledge is required for the Wiener restoration filter, including knowledge of the degradation function as well as the covariance sequences of the original image and noise. Although the Wiener filter is optimally

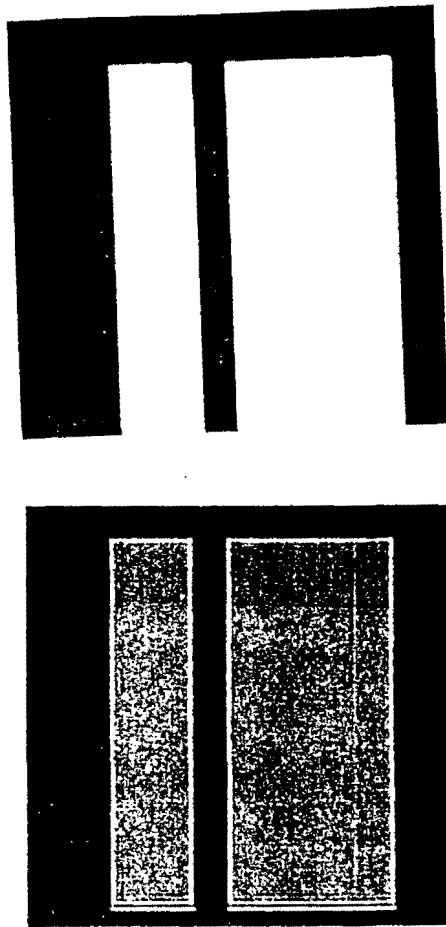


Figure 4.8: Blurred and Wiener filtered images

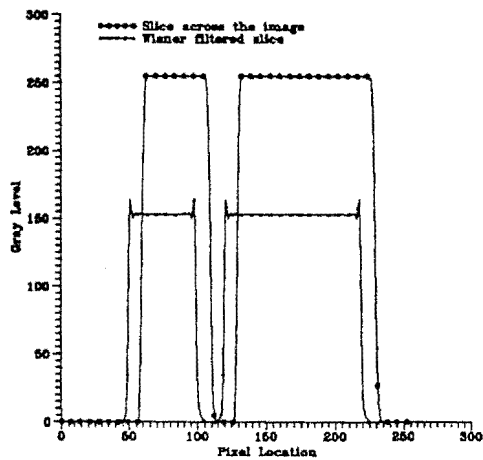


Figure 4.9: Input and Wiener filter processed slice profiles

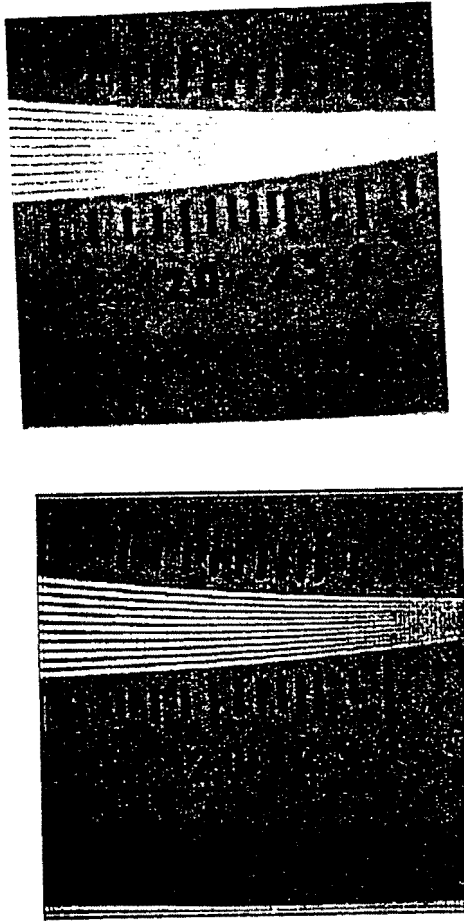


Figure 4.10: Real-time and Wiener filtered images of the resolution gauge

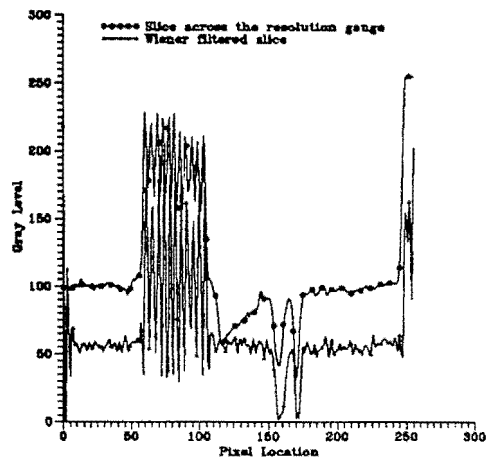


Figure 4.11: Input and Wiener filter processed slice profiles of the resolution gauge

derived, its true success in restoring real-world images depends on accurate estimation of the image and noise covariances.

An initial estimate of the signal covariance can be derived by using the degraded image as a prototype. The estimate can be used to compute the restored image. It is quite plausible that this initially restored image represents a better prototype than the given degraded image, and therefore can be used to obtain a better estimate of the covariance. This suggests an iterative procedure whereby successively restored images are used to update the covariance estimates and subsequently improve the restoration.

For convenience of representation, an image formation model using matrix notation will be used. This is given by

$$g = Hf + n$$

where H represents a linear shift-invariant degradation process, n is an independent white noise process with known variance, f is the ideal image, and g is the observation. If we are dealing with $N \times N$ images, f, g and n are vectors of length N^2 and H is a matrix of $N^2 \times N^2$. The Wiener solution as given earlier can then be written as

$$B = R_{ff}H^t[HR_{ff}H^t + R_{nn}]^{-1}$$

where images are assumed to be zero mean and B is the restoration filter. The solution requires accurate knowledge of R_{ff} , the autocorrelation of f . However, in practical situations, f is usually not available and only a single copy of the blurred image g to be restored is provided. In the absence of a more accurate knowledge of the ideal image f , the blurred image g is often used in its place. The signal g is subsequently used to compute an estimate of R_{gg} and this estimate is used in place

of R_{ff} . The procedure, referred to as the iterative Wiener filter, begins by using the observed image g in place of f to obtain a crude initial estimate of R_{ff} , then by restoring g to \hat{f} using the above equation. Next, the resulting \hat{f} is used to compute a refined estimate of R_{ff} , and subsequently a better \hat{f} . This procedure is repeated iteratively. This procedure can be explained stepwise as follows.

Use g to compute an initial ($i=0$) estimate of R_{ff}

$$R_{ff}(0) = R_{gg} = E(gg^t)$$

Use R_{ff} , the i^{th} estimate of R_{ff} to construct the $(i+1)^{th}$ restoration filter $B(i+1)$ given by

$$B(i+1) = R_{ff}(i)H^t[HR_{ff}(i)H^t + R_{nn}]^{-1}$$

Restore g by the $B(i+1)$ filter to obtain $\hat{f}(i+1)$, the $(i+1)^{th}$ estimate of f

$$\hat{f}(i+1) = B(i+1)g$$

Use $\hat{f}(i+1)$ to compute an improved estimate of R_{ff} , given by

$$R_{ff}(i+1) = E\hat{f}(i+1)\hat{f}^t(i+1)$$

Increment i and repeat the above steps.

The results using this iterative filter are as shown in Figures 4.12 and 4.13 for the simulated image and 4.14 and 4.15 for the resolution gauge.

Iterative Wiener filter with an additive correction factor

The iterative procedure explained in the previous subsection is intuitively reasonable; in the absence of the ideal image f , the filter uses the best available image

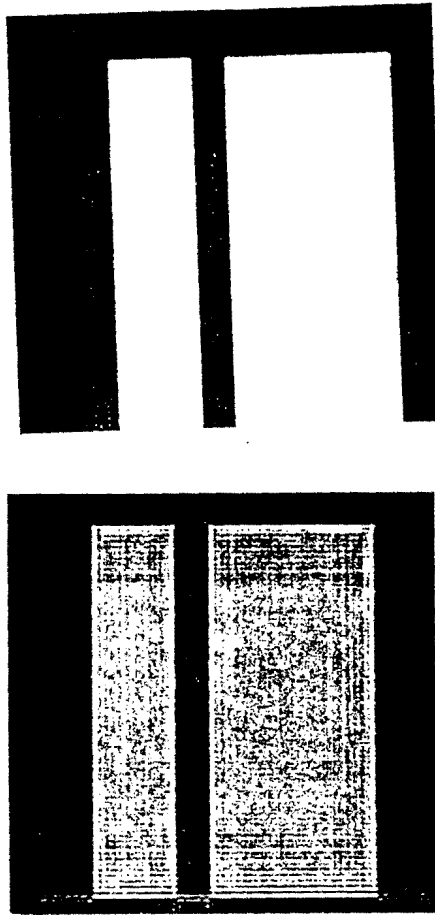


Figure 4.12: Blurred and iterative Wiener filtered images

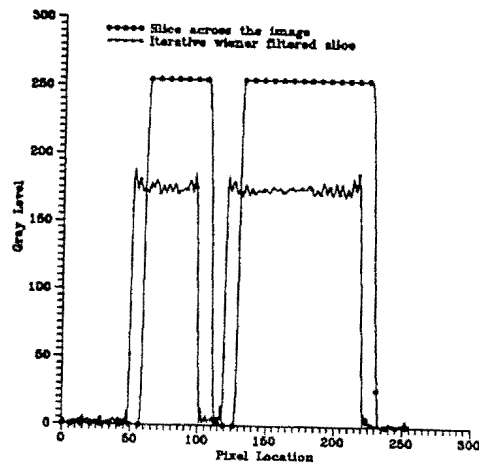


Figure 4.13: Input and iterative Wiener filter processed slice profiles

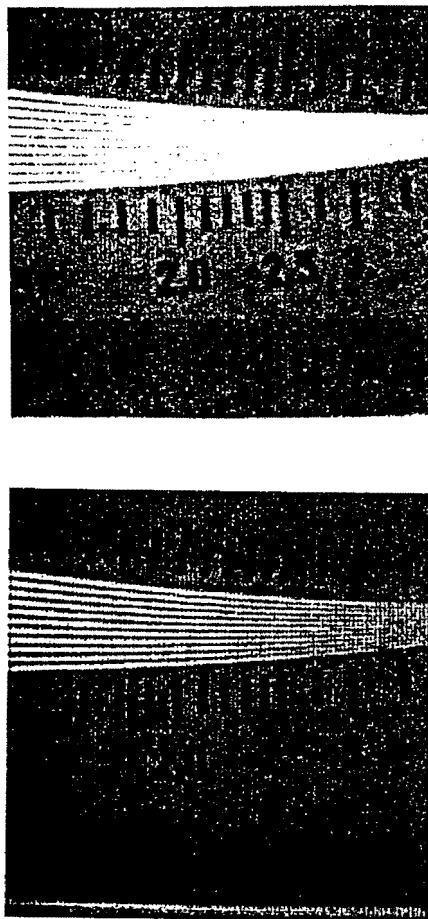


Figure 4.14: Real-time and iterative Wiener filtered images of the resolution gauge

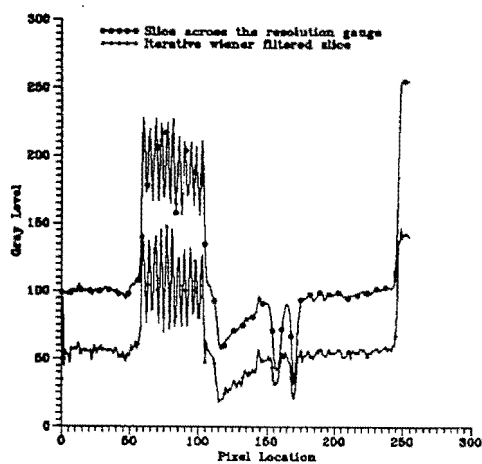


Figure 4.15: Input and iterative Wiener filter processed slice profiles of the resolution gauge

to estimate R_{ff} , and when a better image becomes available it is used to improve the estimate of R_{ff} for restoration. However, the problem with this technique is convergence of the algorithm. Issues of convergence have been addressed by Hillery & Chin (1991). They proposed an additive correction to the iterative filter. This has been implemented here.

The iterative procedure can be modified so that it converges to the true value R_{ff} . A possible modification to is to add a correction term to the new covariance estimate, given by

$$R_{ff}^+(i+1) = R_{ff}(i+1) + S(i+1)$$

where $S(i+1)$ is the correction factor. Instead of estimating the covariance matrix as

$$R_{ff}(i+1) = E\hat{f}(i+1)\hat{f}^t(i+1)$$

the above correction factor is applied. This new estimate of the covariance is used to construct the restoration filter $B(i+1)$. The objective is to correct the error caused by using the restored image \hat{f} instead of the ideal image f for the estimation of $R_{ff}(i+1)$.

The additive correction factor $S(i+1)$ is determined by solving for S at the point where $R_{ff}(i+1) = R_{ff}^+(i) = R_{ff}$

$$S(i+1) = R_{ff}^+(i+1)[I - [B(i+1)H]^t]$$

It has been verified that this additive correction $S(i+1)$ does lead to the ideal value R_{ff} which is a fixed point of the resulting iterative process.

The results using this filter are shown in Figures 4.16 and 4.17 for a simulated image and 4.18 and 4.19 for a resolution gauge.

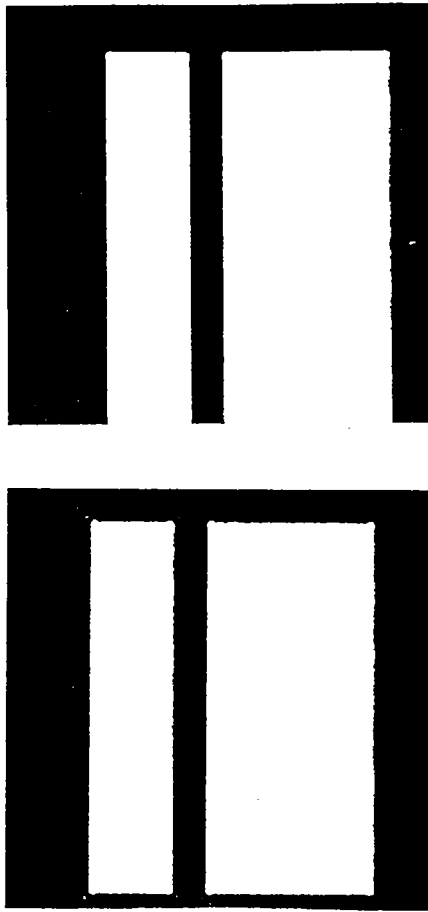


Figure 4.16: Blurred image and a processed image using an iterative Wiener filter with an additive correction factor

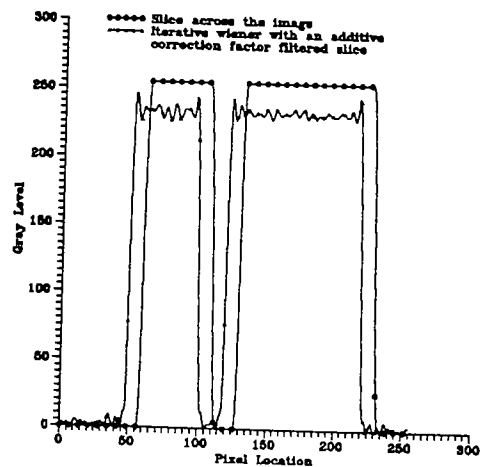


Figure 4.17: Input and iterative Wiener filter with an additive correction processed slice profiles

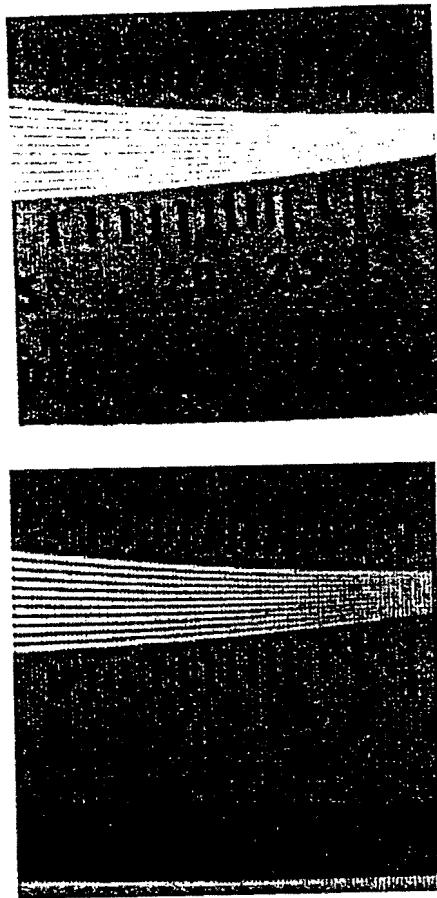


Figure 4.18: Real-time image and a processed image of the resolution gauge using an iterative Wiener filter with an additive correction factor

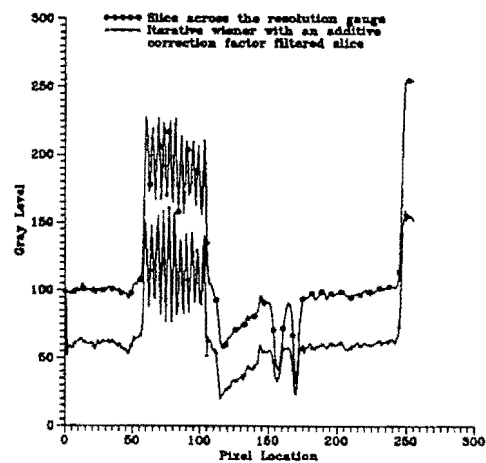


Figure 4.19: Input and Iterative wiener filter with an additive correction factor processed slice profiles of the resolution gauge

A filter based on the EM algorithm

The EM(expectation-maximization) algorithm is a broadly applicable method for calculating maximum likelihood estimates (Hebert, 1989; Levitan, 1987; Chin, 1987). In the EM algorithm, a postulated, unobservable "complete data set" is employed to facilitate the process of maximizing the likelihood function of the measured data. The actual calculation consists of a sequence of alternating expectation steps (the E-step, in which the conditional expectation of a new likelihood function defined on the complete data set is derived) and maximization steps (the M-step, where a set of new estimates is obtained by maximizing the conditional expectation formulated in the E-step). In theory, this iterative process maximizes the likelihood function defined on the measured data. A virtue of maximum likelihood algorithms is the possibility of incorporating every physical and statistical factor involved in the image formation process into a single probability function that is employed in the calculations. In addition, since stationarity is not a necessary condition in EM algorithms, some positionally-variant characteristics of these physical and statistical factors can be compensated for in the reconstruction or processing steps. Therefore, in principle, EM algorithms can produce more accurate images.

The basic idea of the EM algorithm is outlined only briefly here. Detailed descriptions can be found in the literature (Dempster, 1977; Shepp, 1982). Let Y be the random vector that represents the observed data in a study, with a joint probability density function, or likelihood function, $g_L(Y|\lambda)$, where λ is the unobserved parameter vector to be estimated. Maximizing $g_L(Y|\lambda)$ with respect to λ yields the parameter vector estimate with which the data are most consistent. The computations associated with this maximization step may be difficult, however the EM

algorithm generally employs a postulated, unobserved random vector X , called the "complete data set", which is sampled from a larger or richer space, to facilitate the maximization process. X and its likelihood function $q_L(X|\lambda)$ can be related to the observed data Y , now called the "incomplete data set", and its likelihood function $g_L(Y|\lambda)$ by

$$Y = h(X), \text{ and}$$

$$g_L(Y|\lambda) = \int q_L(X|\lambda) d\sigma(X),$$

where h is a many-to-one mapping function that describes the relationship between X and Y , and σ is a measure relating q_L to g_L . As stated before there are two steps corresponding to each iteration of the EM algorithm, an E-step and an M-step. In the E-step, a conditional expectation is formulated by defining

$$Q_E(\lambda|\lambda^n) = E[\ln q_L(X|\lambda)|Y, \lambda^n],$$

where $E[.]$ denotes the expectation value, $\ln q_L$ is the natural logarithm likelihood function, and λ^n are the current (n^{th}) estimates. In the M-step that follows, this conditional expectation is maximized with respect to λ , with λ^n held fixed, to yield a formulation for the calculation of the new $[(N+1)^{st}]$ estimates, λ^{n+1} . Therefore, the original task of maximizing $g_L(Y|\lambda)$ is carried out by many two-step (i.e E-step and M-step) calculations involving $q_L(X|\lambda)$ in an attempt to approach the maximum of $g_L(Y|\lambda)$ iteratively. In other words, repetitive formulation and maximization of $Q_E(\lambda|\lambda^n)$ by an E-step and then an M-step is equivalent to maximizing $g_L(Y|\lambda)$ through an iterative process that asymptotically approaches the maximum likelihood solution.

When applying the EM algorithm to image restoration, $\{Y_{ij}\}$ represents the elements of the degraded image, $\{\lambda_{ij}\}$ represents the elements of the ideal image

and $\{X_{ij}\}$, can be defined as the image intensity or density contributed by λ_j and registered in Y_i . It should be noted that $\{X_{ij}\}$ cannot be measured physically. The relation between the complete data set and the incomplete data set can be written explicitly as

$$Y_i = \sum_j X_{ij}$$

The expectation value of X_{ij} , given λ , can be written as

$$N_{ij} \equiv E[X_{ij}|\lambda] = C_{ij}\lambda_j$$

where C_{ij} is the probability that an event emitted from λ_j would be detected in Y_i . In image restoration $\{C_{ij}\}$ is the transformation matrix that represents the characteristics of the image system in use and the image formation process involved. Using these initial values and applying the EM algorithm, Chin & Metz (1987) have derived the following equation

$$\lambda_j^{n+1} = \lambda_j^n / (\sum_j C_{ij}) \cdot \{ \sum_i C_{ij} [Y_i / (\sum_k C_{ik} \lambda_k^n)] \}$$

To apply this algorithm for image restoration the elements of $\{C_{ij}\}$ were taken as the PSF of the system, the elements of $\{Y_{ij}\}$ were those of the degraded image and the degraded image was also chosen as an initial choice for the elements of $\{\lambda_{ij}^0\}$. This value of λ was used to get a new estimate.

The results obtained after 3 iterations of the EM algorithm are shown in Figures 4.20, 4.21 for the simulated image and 4.22 and 4.23 for the resolution gauge.

FIER MEM filter

The Maximum Entropy Method (MEM) has been widely used for the restoration of radiographic images. It was introduced by Jaynes to estimate probability functions and has been used by many authors, including Burg (1969) , Frieden (1972) and



Figure 4.20: Blurred and EM filtered images

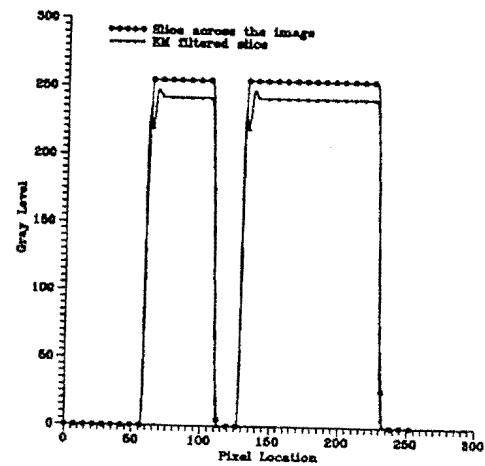


Figure 4.21: Input and EM filter processed slice profiles



Figure 4.22: Real-time and EM filtered images of the resolution gauge

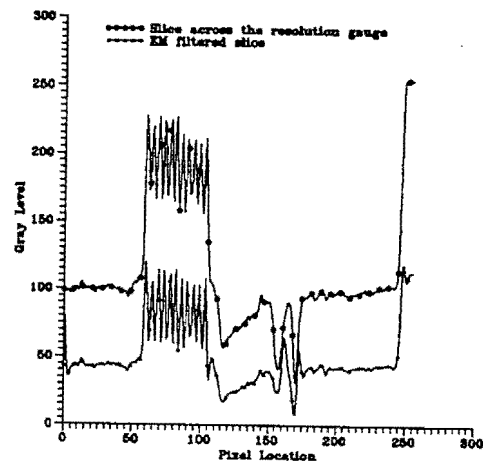


Figure 4.23: Input and EM filter processed slice profiles of the resolution gauge

Burch, Gull and Skilling (1983) in a variety of applications. The method balances two conflicting requirements: to maximize the entropy of an (estimated) object and to minimize the mean square error between the observed data and reconstructed data based on the object. The formulation leads to a nonlinear, implicit equation which the object must satisfy and the ME methods solve the equation, usually by an iterative process.

Most methods start with a flat featureless object, the unconstrained object with maximum entropy, and modify this estimate to achieve the desired balance between entropy and the error. Gonsalves et al.(1990) have used the Wiener filtered image as the starting estimate, an estimate which is modified iteratively to achieve a desired error while, at each iteration, the entropy is increased. The search direction is a filtered entropy gradient; so the approach is called FIER, for Filtered Entropy Restoration. The procedure developed by Gonsalves et al has been implemented here and is outlined in the following section. The image formation model is given by the expression

$$D = HO + N$$

where D is a $K \times 1$ degraded image vector, H is the $K \times J$ PSF matrix, O is the $J \times 1$ ideal image vector and N is the $K \times 1$ noise vector. The problem is to estimate O based on D , with a knowledge of H . The estimate is F , a $J \times 1$ vector.

The entropy of F is defined as

$$e = - \sum_{j=1}^J (f(j)/c) \ln(f(j)/c)$$

where c is the area of F

$$c = \sum_{j=1}^J f(j)$$

The mean square error, m is found by constructing an estimate, G of the data:

$$G = HF$$

Then

$$m = \sum_{k=1}^K (d(k) - g(k))^2 = |D - HF|^2$$

The problem is to find an estimate, F , which maximizes the entropy, e , while constraining the mean square error, m to be some fixed m_0 . To find a solution vector F , a metric, q is set up given by

$$q = e - am$$

where a is a scalar weighting factor. Then F must have elements $f(j)$ which satisfy

$$\frac{\partial q}{\partial f(j)} = 0$$

or, we can write

$$\frac{\partial e}{\partial f(j)} = a \frac{\partial m}{\partial f(j)}, \forall j$$

In vector form, the entropy gradient V , must be proportional to the mean square error gradient W , Thus we have

$$V = aW$$

To find the elements of V we differentiate the entropy e with respect to $f(j)$. This yields, after considerable algebra,

$$v(j) = \frac{\partial e}{\partial f(j)} = -(e + \ln(f(j)/c))/c$$

The elements of W are found by differentiating, m with respect to $f(j)$. This gives

$$w(j) = \frac{\partial m}{\partial f(j)} = -2 \sum_{k=1}^K (d(k) - g(k))h(k, j),$$

or, for the vector W we can write directly,

$$\begin{aligned} W &= -2H^T(D - G) \\ &= -2H^T(D - HF) \end{aligned}$$

Substituting this value of W , we have

$$V = -2aH^T(D-HF),$$

The above equation is an implicit equation for F , since F appears on the right and $\ln f(j)$ appears on the left hand side.

Holding V fixed, we can solve the above equation for F , i.e.,

$$(H^T H) F = H^T D + V / (2 a)$$

If $R = H^T H$ has an inverse, F can be solved to get

$$F = R^{-1}H^T D + R^{-1}V / (2 a)$$

A new scalar multiplier is defined $s = 1/(2a)$ and a vector B

$$B = R^{-1}V$$

Then the above equation can be written as

$$F = R^{-1}H^T D + s B, \text{ a solution for } F.$$

If R is not full rank, it will not have an inverse. This is guarded against by adding a small positive constraint, Z to the diagonal of R . Thus

$$R = H^T H + Z I,$$

where I is the identity matrix. Z is a noise control parameter. From the equation for F , we can see that the first term is a generalized Wiener filter. This becomes evident if we take the Fourier transform of the first term. This gives

$$F(m) = \frac{H^*(m)D(m)}{H^*(m)H(m)+Z}$$

The second term in the equation for F has two parts: s , a scalar, and B , a vector. The vector B , is the entropy gradient V , filtered by the inverse of R . Again computing

the Fourier transform on both sides,

$$B(m) = \frac{V(m)}{H^*(m)H(m)+Z}$$

Thus B is a filtered entropy gradient. The n^{th} iteration of F can be now be expressed as

$$F^{(n)} = F^{(n-1)} + sB,$$

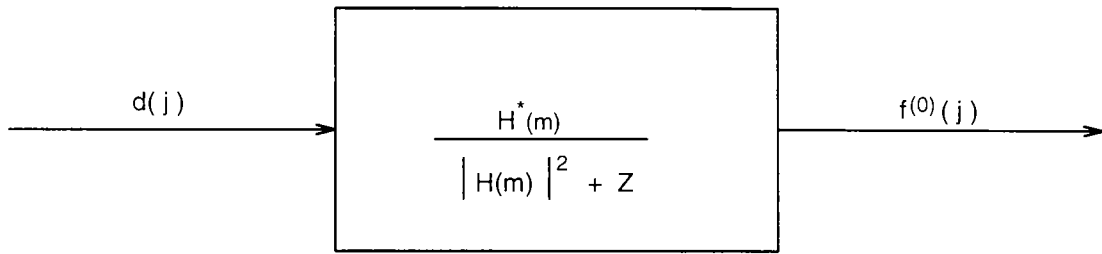
where

$$F^{(0)} = R^{-1}H^TD$$

Thus the algorithm starts with an initial Wiener estimate, calculates the filtered entropy gradient, B , for that estimate, and steps a distance s in direction B to get $F^{(1)}$. The iterations continue until the process converges to a solution vector F .

A block diagram of the algorithm is as shown in the figure 4.24. The data elements $d(j)$ are passed through a Wiener filter to get the initial estimate with elements $f^{(0)}(j)$. The n^{th} iterate has elements $f^{(n)}(j)$, which follow from the above equation. The direction elements $b(j)$ can be obtained by taking the log of $f^{(n-1)}(j)$ and filtering the result as given above. The step size s is calculated depending on the desired MSE, m .

The results using this filter are shown in the figures 4.25 and 4.26 for the simulated image and 4.27 and 4.28 for the resolution gauge. This filter has worked the most efficiently for the restoration of the x-ray images. The reason lies in the fact that this algorithm uses two constraints on the restored image, maximizing the entropy while at the same time keeping a check on the MSE between the true and the restored image. In addition MEM techniques have advantages of positivity of the restored image, minimization of the ringing artifacts and noise sensitivity. A comparison of the various filters is made in the next section.



$$f^{(n)}(j) = f^{(n-1)}(j) + s b(j)$$

s = step size

$b(j)$ = filtered entropy gradient

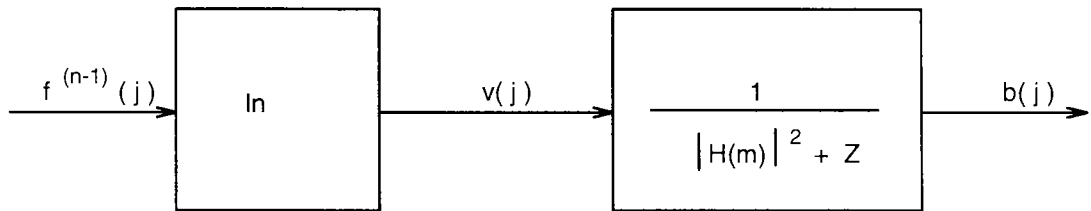


Figure 4.24: Block diagram of the FIER MEM filter

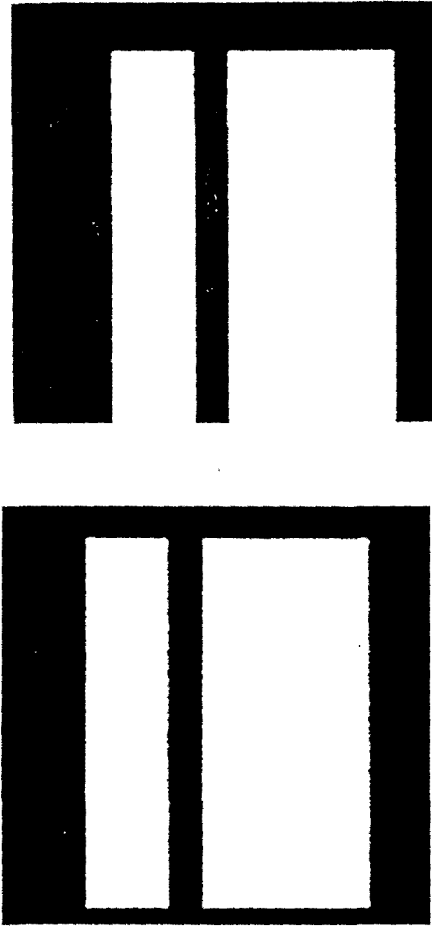


Figure 4.25: Blurred and MEM filtered images

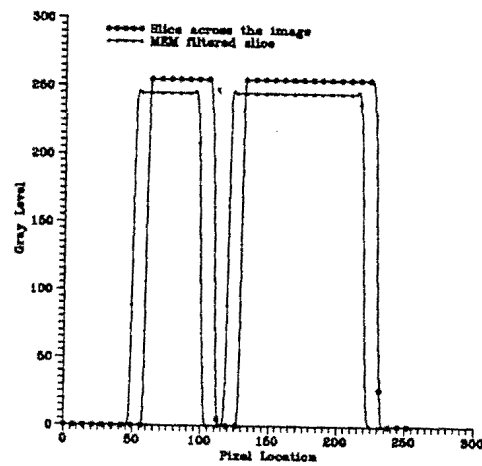


Figure 4.26: Input and MEM filter processed slice profiles

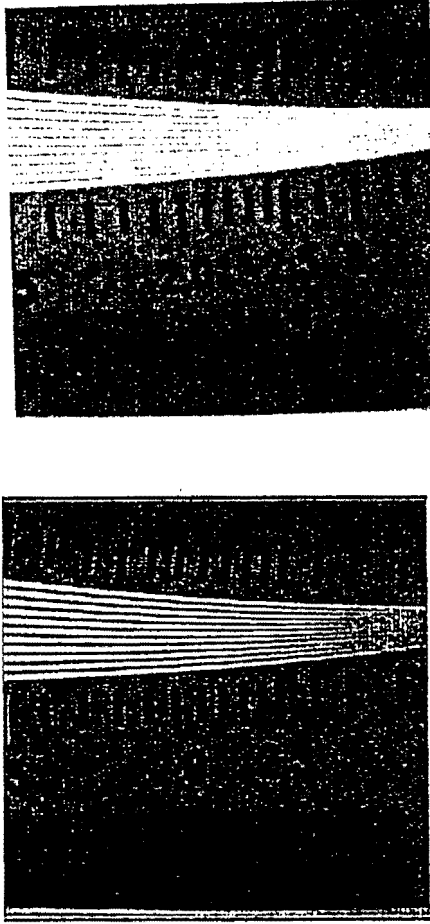


Figure 4.27: Real-time and MEM filtered images of the resolution gauge

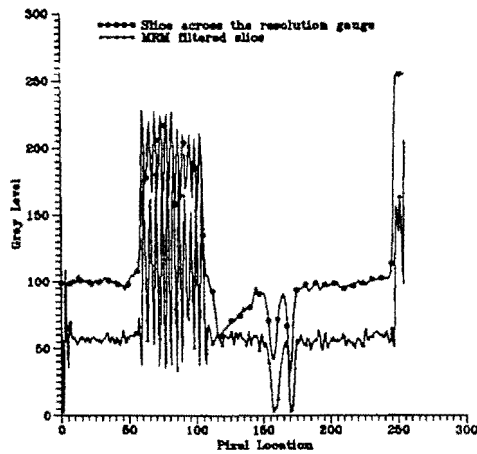


Figure 4.28: Input and MEM filter processed slice profiles of the resolution gauge

Comparison of various filters

The effectiveness of each approach has been evaluated by comparing the filtered images both visually and quantitatively. For the resolution gauge, a quantitative comparison is made by observing an improvement in contrast. A slice at the same row is taken for the degraded and the restored images. The slice from the restored images is offset in these plots to facilitate comparison. These plots are shown in Figures 4.7, 4.11, 4.15, 4.19, 4.23 and 4.28. Using the inverse, EM, the iterative Wiener filter with and without an additive correction factor there is not much improvement in contrast although an improvement can be observed in a visual sense. The reason for the lack of improvement is the noise present in a real time image and as indicated in the previous section this filter doesn't perform well in the presence of noise. The issue of convergence is also a source of concern with the other three filters. Using the Wiener and the MEM filter there is an improvement of about 2.4 in the contrast level. Since the Wiener filter tries to reduce the mean square error between the true and the restored image, an improvement in contrast can be observed. Also since the MEM filter increases the entropy in addition to reducing the mean square error an improvement in contrast can be observed.

Mean square error is another metric technique for the comparison of two images. However in order to be able to do so a true image should be available. Hence this technique is useful only in the case of simulated images. The mean square error between the true and the restored images is calculated for all the filters. From table 4.1 it can be seen that the MEM filter has the lowest mean square error; this means that it is closest in the least square sense to the true image. Also notice the reduction in the mean square error for the iterative method and the iterative method incor-

Table 4.1: Mean Square Error between the ideal and restored images for different filters

Restoration filter	Mean Square Error
Pseudo Inverse	9657.54
Expectation Maximization	9508.58
Wiener	5827.76
Iterative Wiener	3944.19
Additive Iterative Wiener	1047.28
FIER MEM	914.46

porating the additive correction Wiener filter as compared to the standard Wiener filter.

CHAPTER 5. CONCLUSIONS AND FUTURE WORK

In this thesis two different yet complementary techniques have been developed. One, a quantitative model for a real-time X-ray imaging system has been developed and the other, procedures to improve the image quality of an image-intensifier based system have been developed. In particular, various deconvolution techniques for X-ray images have been studied.

Having a quantitative model can help in understanding the physics of the underlying image formation process. The understanding of the image generation process and the distortions introduced by the system are a prerequisite to the deconvolution of deterministic processes and the extraction of information from the image.

Treating the system as a combination of two different subsystems one consisting of just the X-ray generator and the image intensifier and the other just the imaging subsystem helped in separating the physics of the image intensifier from that of the imaging system. Two important conclusions were arrived at adopting this strategy. One, the sensitivity of the image intensifier varies significantly under different operating kvp conditions and second, that different cameras have different calibration curves. In addition it was observed that although the image intensifier is capable of offering higher resolution, we are limited by the resolution (8 bits) of the CCD camera.

Also, there is a trade-off between the field of view (FOV) and the spatial resolution of the imaging system. This was verified by using the model for the real-time imaging system. Since the model allows variable pixel sizes, the field of view of an object can be changed easily. Two different views of a circular gauge were used to verify the trade-off. Figure 5.1 shows the image of a circular gauge with a pixel size of 0.086mm/pixel (larger field of view) and Figure 5.3 shows the image of the same object with a smaller pixel size of 0.047mm/pixel (smaller field of view). Figures 5.2 and 5.4 are the deconvolution results of these two images respectively. It can be seen that Figure 5.4 has a greater resolution than Figure 5.2. This implies that the deconvolution routine was able to improve the quality of an image more effectively when a smaller field of view was used. This verifies the trade-off between the spatial resolution and the FOV.

Various deconvolution techniques were applied to improve the quality of X-ray images. There was an improvement of resolution from 1.5 lp/mm to about 3 lp/mm for the resolution gauge. Additional improvement was not possible due to the limitations of the optics involved. The MEM filter, which has been traditionally used for the restoration of X-ray images, did a better job of blur removal while at the same time minimizing the ringing artifacts and noise. In addition using the Wiener filter estimate as the initial estimate of the image instead of using a flat featureless image prevents the algorithm from getting trapped in a local minima. The various deconvolution routines were developed with an aim to obtain the maximum possible resolution at the maximum field of view.

The model for the real-time system was developed based on a similar model developed for film radiography. The model is significantly robust to take care of

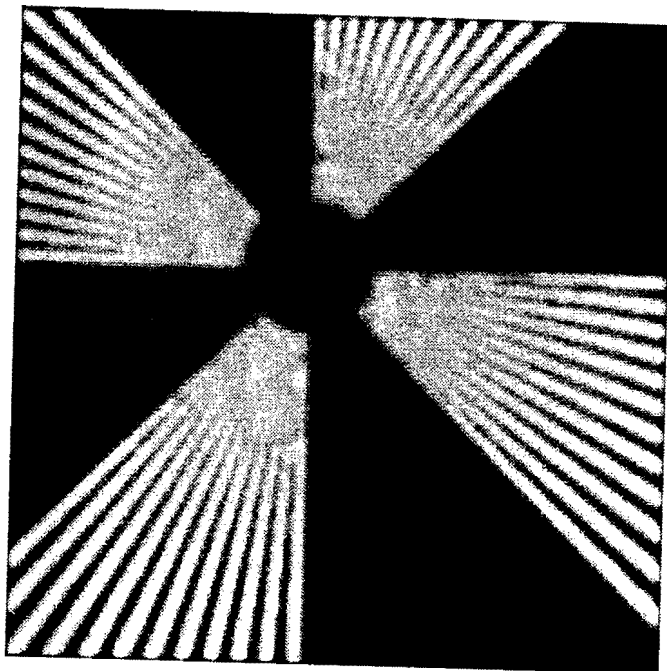


Figure 5.1: Image of a circular gauge with a larger field of view

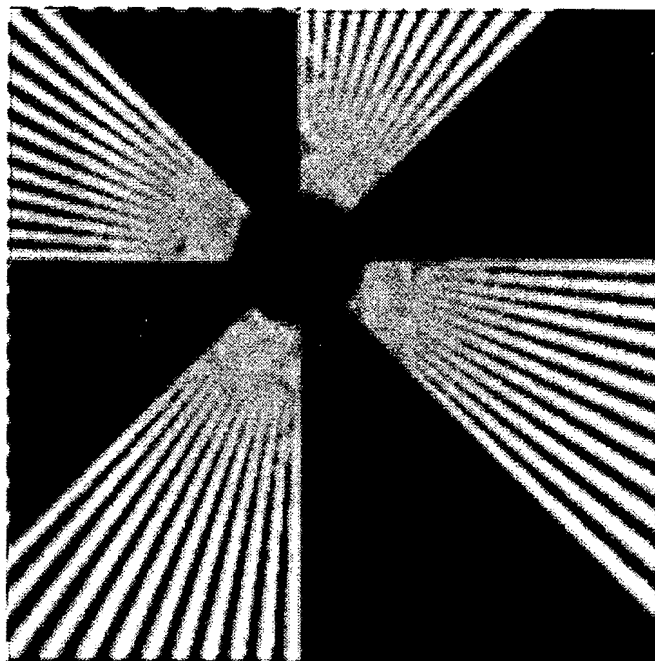


Figure 5.2: Deconvoluted image of a circular gauge with a larger field of view

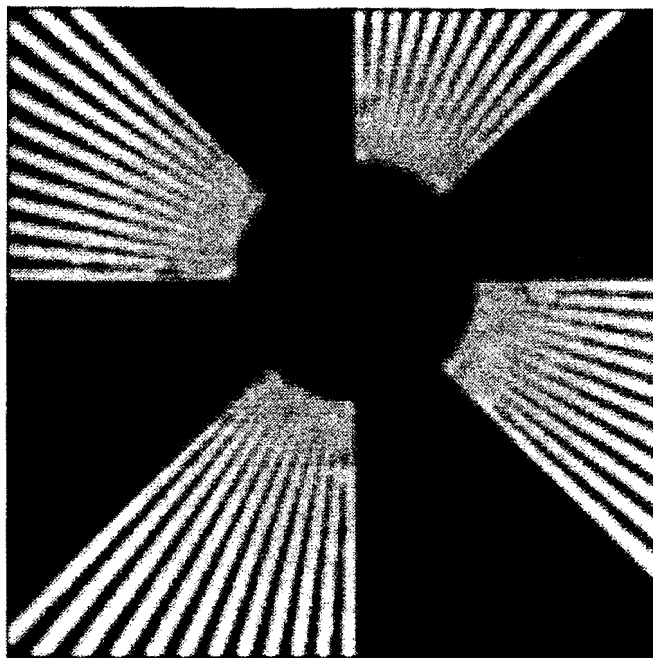


Figure 5.3: Image of a circular gauge with a smaller field of view

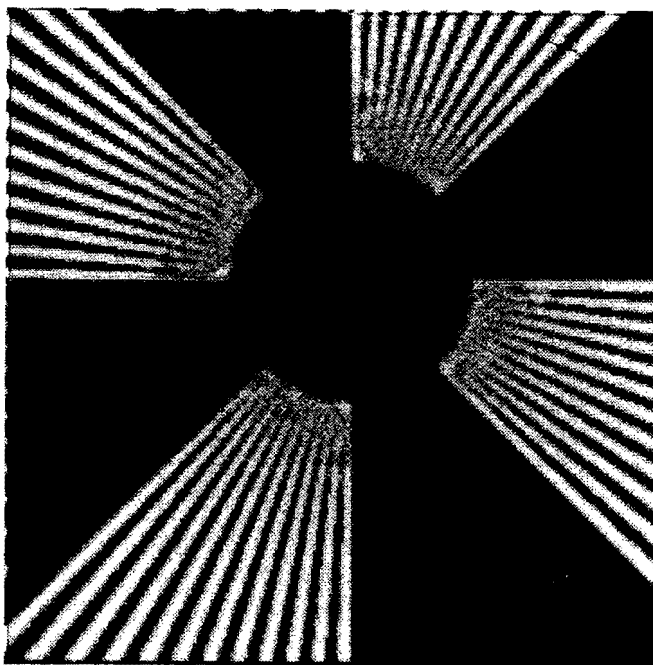


Figure 5.4: Deconvoluted image of a circular gauge with a smaller field of view

various distortions involved in the image formation process. The PSF was measured experimentally using a new technique and was incorporated into the model. This PSF accounts for the phosphor bloom of the image intensifier and the blurring due to the camera MTF. The distortion introduced by the curved input surface of the image intensifier screen was also measured and incorporated into the model. Finally Poisson noise was added to make the simulated image as close as possible to that of a real-time image. This model can be used in a wide variety of image processing applications.

Ideas for future work

In estimating the PSF of the system, it would be of interest to separate the PSF representing the phosphor bloom of the image intensifier from that of the camera MTF and observe the effect both on the image restoration routines and the model. Pincushion distortion is presently incorporated for a fixed source- detector geometry. This could be extended to a variable source-detector arrangement to take into account view-dependent distortion. The noise as it is incorporated currently is derived by comparing the simulated and real-time image. Hence, better techniques for noise estimation of real-time images should be investigated. The main drawback with the current model for image processing applications is image registration. Unless there is high degree of correspondence between the simulated and real-time image, the model cannot be used for image processing applications effectively. Future work can examine new methods for image registration. Since we have an access to the ideal image enough *a priori* information can be obtained from the image. The *a priori* information can be used to develop efficient image restoration algorithms.

BIBLIOGRAPHY

- Andrews, H. C., and B. R. Hunt. 1977, Digital image restoration, Prentice-Hall, Englewood Cliffs, NJ.
- Bates, C. W., Jr. 1980, Concepts and implementations in X-ray intensification, Pages 45–65 in D. A. Garrett and D. A. Bracher, eds. Real-time radiologic imaging: medical and industrial applications, American Society for Testing and Materials, Philadelphia, PA.
- Burch, S. F., S. R. Gull, and J. Skilling, 1983, Image restoration by a powerful maximum entropy method, *Comp. Vision, Graph., Image Proc* 23:113-128.
- Burg, J. P., , 1960. Maximum entropy spectral analysis, 37th Meeting, Soc. of Exploration Geophysicists (Oklahoma City, OK).
- Casperson, L. W., P. Spiegler, and J. H. Grollman, Jr. 1976, Characterization of aberrations in image-intensified fluoroscopy, *Medical Physics* 3(2):103–106.
- Chakraborty, D. P. 1987, Image intensifier distortion correction, *Medical Physics* 14(2):249–252.
- Chalmeton, V. 1980, Microchannel X-ray image intensifiers, Pages 66–89 in D. A. Garrett and D. A. Bracher, eds. Real-time radiologic imaging: medical and industrial applications, American Society for Testing and Materials, Philadelphia, PA.
- Chin-Tu C., and Charles E. Metz, 1987, Application of EM algorithm in image reconstruction and image processing, *SPIE Vol. 767 Medical Imaging*:326-331.
- Christensen, E. E., T. S. Curry, III, and J. Nunnally. 1972, An introduction to the physics of diagnostic radiology, Lea and Febiger, Philadelphia, PA.

- Csorba, I. P. 1985. Image tubes, Howard W. Sams and Co., Indianapolis, IN.
- Dempster, A.P., Laird, N. M. and Rubin, D. B., 1977, Maximum Likelihood from Incomplete Data via the EM algorithm, JRSS, 39: 1-38.
- Doering, E. R., J. N. Gray, and J. P. Basart, 1992. Point spread function estimation of image intensifier tubes, Pages 323-329 in D. O. Thompson and D. E. Chimenti, eds. Review of Progress in Quantitative NDE Vol. 11A, Plenum Press, New York.
- Doering, E. R. 1992, Three-dimensional flaw reconstruction using a real-time X-ray imaging system, PhD dissertation, Iowa State University, Ames, IA.
- Frieden, B. R., 1972, Restoring with maximum likelihood and maximum entropy, J. Opt. Soc. Am. 62(4): 511-518.
- Glasser, J., J. Vaillant and F. Chazallet. 1988, An accurate method for measuring the spatial resolution of integrated image sensors, Image Processing II, SPIE 1027:40-47.
- Gray, J. N., 1988, Three dimensional modeling of projection x-ray radiography, Pages: 343-348 in D. O. Thompson and D. E. Chimenti, eds. Review of Progress in Quantitative NDE Vol. 7A, Plenum Press, New York.
- Gray, J. N., and F. Inanc and B. E. Shull, 1989, Three dimensional modeling of projection radiography, Pages: 345-350 in D. O. Thompson and D. E. Chimenti, eds. Review of Progress in Quantitative NDE Vol. 8A, Plenum Press, New York.
- Gray, J. N., and F. Inanc, 1990, A CAD interfaced simulation tool for x-ray NDE studies, Pages: 391-398 in D. O. Thompson and D. E. Chimenti, eds. Review of Progress in Quantitative NDE Vol. 9A, Plenum Press, New York.
- Gonsalves, R. A., J. P. Kennealy, R. M. Korte, and S. D. Price. 1990, FIER: A filtered entropy approach to maximum entropy image reconstruction, Pages 369-382 in P. F. Fougère, ed. Maximum Entropy and Bayesian Methods. Kluwer Academic Publishers, Boston, MA.
- Gupta, N. K., and B. R. Krohn. 1987, Discrete detectors for near-real-time radiography, Materials Evaluation 45:1320-1325.

- Haaker, P., E. Klotz, R. Koppe, and R. Linde. 1988, Real-time distortion correction of digital X-ray II/TV systems: an application example, *Image Processing II*, SPIE 1027:261-266.
- Halmshaw. R. 1987, An analysis of the performance of X-ray television-fluoroscopic equipment in weld inspection. *Materials Evaluation* 45:1298-1302.
- Hebert, T. and L. Richard. 1989. A Generalized EM algorithm for 3-D Bayesian Reconstruction from Poisson Data Using Gibbs Priors, *IEEE Transactions on Medical Imaging*. 8(2):194-202.
- Hillen, W., U. Schiebel, and T. Zaengel. 1987, Imaging performance of a digital storage phosphor system, *Medical Physics* 14(5):744-751.
- Hillery, A. D, and Roland T. Chin, 1991, *IEEE transactions on signal processing*. 39:1892-1899.
- Jain, A. K. 1989. *Fundamentals of Digital Image Processing*, Prentice-Hall, Englewood Cliffs, NJ.
- Lee, C.M, L. Kissell, R.H. Pratt, H.K. Tseng, 1976, *Phys. Rev.* A13(5):1714-1727.
- Leviton. E., and Gabor T. Herman, 1987, A Maximum A Posteriori Probability Expectation Maximization Algorithm for Image Reconstruction in Emission Tomography, *IEEE Transactions on Medical Imaging*, MI-6(3):185-192.
- Link, R., W. Nuding, H. Wiacker, H. P. Busse, and J. J. Munro, III. 1989, Weld inspection using real-time radiography, *International Advances in Nondestructive Testing* 14:143-173.
- Macovski. Albert. 1983, *Medical Imaging*, Prentice-Hall, Englewood Cliffs, NJ.
- Parzen, E. 1960, *Modern Probability Theory and its applications*, John Wiley & Sons, New York.
- Press, W. H., B. P. Flannery, S. A. Teukolsky, and W. T. Vetterling. 1988, *Numerical recipes in C: the art of scientific computing*, Cambridge University Press, New York, NY.
- Samuelson, E. G., and B. Jaggi. 1989, Design and implementation of a solid state imaging system for visible light and X-ray imaging, Pages 393-394 in *proceedings of the 11th Annual International Conference of the IEEE*

- Engineering in Medicine and Biology Society, Part 2. Alliance for Engineering in Medicine and Biology, Washington, DC.
- Seibert, J. A., O. Nalcioglu, and W. W. Roeck. 1984, Characterization of the veiling glare PSF in X-ray image intensified fluoroscopy, *Medical Physics* 11(2):172-179.
- Shepp, L.A., and Y. Vardi, 1982, Maximum Likelihood Reconstruction for Emission Tomography. *IEEE transactions on Medical Imaging*, MI-1(2):113-122.
- Williams, C. S. 1989, Introduction to the optical transfer function. Wiley. New York.
- Zhu, Y. M., D. Babot, and G. Peix. 1990, A quantitative comparison between linear X-ray sensitive array and image-intensifier systems, *NDT International* 23(4):214-220.